

Article

Flipping the Switch: Fast Photoisomerization in a Confined Environment

Derek E. Williams, Corey R Martin, Ekaterina A. Dolgoplova, Anton Swifton, Danielle C Godfrey, Otega A. Ejegbavwo, Perry J Pellechia, Mark D. Smith, and Natalia B. Shustova

J. Am. Chem. Soc., **Just Accepted Manuscript** • Publication Date (Web): 28 May 2018

Downloaded from <http://pubs.acs.org> on May 28, 2018

Just Accepted

“Just Accepted” manuscripts have been peer-reviewed and accepted for publication. They are posted online prior to technical editing, formatting for publication and author proofing. The American Chemical Society provides “Just Accepted” as a service to the research community to expedite the dissemination of scientific material as soon as possible after acceptance. “Just Accepted” manuscripts appear in full in PDF format accompanied by an HTML abstract. “Just Accepted” manuscripts have been fully peer reviewed, but should not be considered the official version of record. They are citable by the Digital Object Identifier (DOI®). “Just Accepted” is an optional service offered to authors. Therefore, the “Just Accepted” Web site may not include all articles that will be published in the journal. After a manuscript is technically edited and formatted, it will be removed from the “Just Accepted” Web site and published as an ASAP article. Note that technical editing may introduce minor changes to the manuscript text and/or graphics which could affect content, and all legal disclaimers and ethical guidelines that apply to the journal pertain. ACS cannot be held responsible for errors or consequences arising from the use of information contained in these “Just Accepted” manuscripts.

Flipping the Switch: Fast Photoisomerization in a Confined Environment

Derek E. Williams,^{‡a} Corey R. Martin,^{‡a} Ekaterina A. Dolgoplova,^{‡a} Anton Swifton,^b Danielle C. Godfrey,^a Otega A. Ejegbavwo,^a Perry J. Pellechia,^a Mark D. Smith,^a and Natalia B. Shustova^{a*}

^aDepartment of Chemistry and Biochemistry, University of South Carolina, Columbia, South Carolina 29208, United States

^bDepartment of Mathematics, University of South Carolina, Columbia, South Carolina 29208, United States

ABSTRACT: Stimuli-responsive materials are vital for addressing emerging demands in the advanced technology sector as well as current industrial challenges. Here, we report for the first time that coordinative integration of photoresponsive building blocks possessing photochromic spiropyran and diarylethene moieties within a rigid scaffold of metal-organic frameworks (MOFs) could control photophysics; in particular, cycloreversion kinetics with the level of control, which is not accessible in the solid state or solution. On the series of photoactive materials, we demonstrated for the first time that photoisomerization rates of photochromic compounds could be tuned within almost two orders of magnitude. Moreover, cycloreversion rates of photoresponsive derivatives could be modulated as a function of the framework structure. Furthermore, through MOF engineering we were able to achieve complete isomerization for coordinatively immobilized spiropyran derivatives, typically exhibiting limited photoswitching behavior in the solid state. For instance, spectroscopic analysis revealed that the novel monosubstituted spiropyran derivative grafted to the backbone of the MOF pillar exhibits a remarkable photoisomerization rate of 0.16 s^{-1} , typical for cycloreversion in solution. We also applied the acquired fundamental principles towards mapping of changes in material properties, which could provide a pathway for monitoring material aging or structural deterioration.

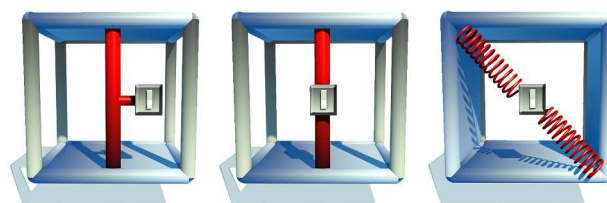
INTRODUCTION

Photochromic building blocks capable of switching between two discrete states upon external stimuli are vital for applications such as “smart” windows, transition lenses, optical switches, or controlled drug delivery systems mainly due to the drastic difference in the photoisomer properties.^{1–14} For instance, upon changing excitation wavelength, temperature, pressure, or pH, a material absorption/emission profile, dielectric constant, or reduction potential could be drastically modulated.^{15–21}

Due to the tunability and multifaceted modularity of metal-organic frameworks (MOFs),^{22–44} photochromic derivatives could be embedded into a framework through different pathways: inside the pores or as linkers (or a part of a linker).^{45–53} In this work, we developed a novel synthetic methodology in combination with recent advances in the MOF field^{54–80} to probe photophysics of photochromic compounds in a confined environment defined by framework topology (Scheme 1). We attempted for the first time to gain fundamental knowledge of cycloreversion kinetics (i.e., transition between two states upon radiation with visible light) of two distinct classes of photochromic compounds with spiropyran- and diarylethene cores in the solid state, solution, and coordinatively immobilized inside the rigid matrix. For that, we prepared novel spiropyran derivatives with anchors for metal coordination, which resulted in the first example of a spiropyran-based MOF

Scheme 1. A schematic representation of coordinatively immobilized photochromic derivatives inside the metal-organic rigid scaffold. The photochromic moiety integrat-

ed as (left) a side group on the organic linker, (middle) as a framework backbone, and (right) as a capping linker⁷⁷ with the size similar to the framework pocket. A grey “photoswitch” symbol indicates a position of a photochromic unit.



with a photochromic unit as a side group on the linker backbone. Such coordinative immobilization of photochromic derivatives inside a scaffold allowed us to study the possibility of tuning photoisomerization rates as a function of framework topology with a level of control that is not accessible in the solid state or solution. We have investigated five systems, which provide us different pathways for anchoring of photochromic compounds to allow for tunability of rigidity and photoswitching capacity. In our studies, we were also able to investigate the effect of steric hindrance on photoswitching ability. As a result, the acquired fundamental principles were applied towards mapping the changes of material properties, which provide a pathway for utilization of the introduced concept towards development of stimuli-responsive markers.

RESULTS AND DISCUSSION

The Result and Discussion section includes the following subsections: (1) synthesis and study of photochromic compounds; (also includes characterization of diastereoisomer equilibration kinetics for one of the novel ligands bearing two photoswitchable units) (2) design and preparation of frameworks for integration of synthesized photochromic compounds, highlighting benefits of framework structural tunability (Scheme 1) including structural analysis; (3) photoisomerization kinetics of photochromic molecules in the solid state and solution as well as after their incorporation inside a rigid scaffold; (4) mapping changes of material properties through utilization of a prepared photochromic scaffold.

Comprehensive analysis of the frameworks and their precursors includes single-crystal and powder X-ray diffraction (PXRD), solid-state and solution nuclear magnetic resonance (NMR), Fourier transform infrared (FTIR), steady-state fluorescence, diffuse reflectance, UV-vis spectroscopies, and mass spectrometry, which will be discussed for each respective system.

Synthesis of Photochromic Linkers

To build novel stimuli-responsive frameworks with coordinatively immobilized photoswitchable units, we prepared four different photochromic molecules belonging to two distinct classes (Figures 1–3). Photochromic linkers with a diarylethene core were chosen due to their fatigue-resistant photochromic performance, thermal stability, and rapid response in the solid state (Figure 1).^{78–81} For coordinative immobilization inside the framework, the photoswitchable core was modified with pyridyl groups or carboxylic acid arms to facilitate coordination to metal centers. The diarylethene derivatives, 1,2-bis(2-methyl-5-(pyridin-4-yl)thiophen-3-yl)cyclopent-1-ene (BPMTC) and 4,4'-(cyclopent-1-ene-1,2-diyl)bis(5-methylthiophene-2-carboxylic acid) (H₂BCMTC) are shown in Figure 3.^{82,83}

As the second class of photochromic linkers, we chose spiroopyran derivatives due to the different pathway of the photoinduced cyclization reaction in comparison with diarylethene derivatives (Figure 1). In contrast to diarylethenes, which isomerization could be described by covalent bond formation between the methylthiophene groups,⁸⁴ spiroopyran-based compounds undergo relatively large structural changes centered on the *sp*³ “spiro”-carbon, rotating from orthogonal to planar geometry (Figure 1).^{3,85,86} Moreover, spiroopyran is hydrophobic and uncharged, whereas its colored isomer, merocyanine, is a hydrophilic zwitterion (Figure 1).⁸⁷ Furthermore, diarylethene-based compounds are capable of 100% reversible photoisomerization in the solid state,⁸⁸ while spiroopyran derivatives do not typically lead to solid-state reversible photoisomerization due to the necessary large structural reorganization.⁸⁹ In general, solid-state spiroopyran photoisomerization has been explored for derivatives tethered to solid supports.⁹⁰ Therefore, there is a demand to systematically create solid-state spiroopyran-based materials to

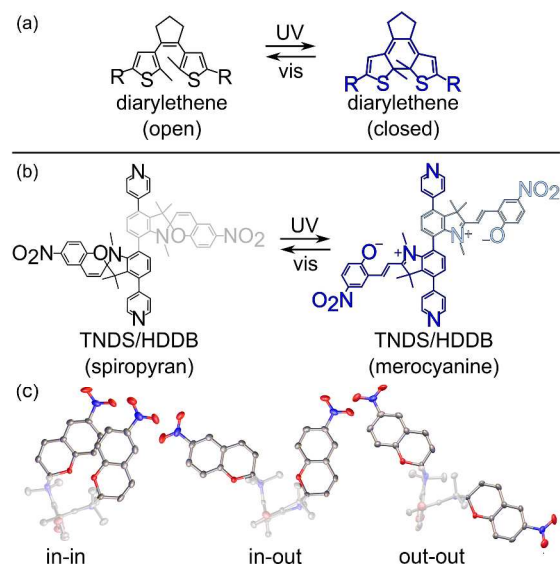


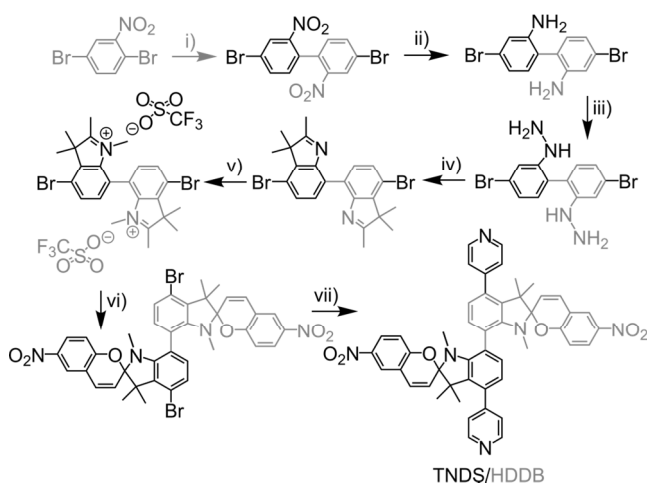
Figure 1. (a) Photoisomerization of the diarylethene-based and (b) spiroopyran derivatives. (c) For simplicity, structural differences of “in-in”, “in-out”, and “out-out” diastereoisomers are shown on the example of the brominated precursor (Scheme 2)⁹¹ of HDDB. Displacement ellipsoids drawn at the 60% probability level. Gray, blue, and red spheres represent C, N, and O atoms, respectively.

harness full potential of spiroopyran derivatives in advanced technologies.

To overcome such steric hindrance observed for spiroopyran groups in the solid state, we synthesized two novel photochromic linkers with spiroopyran groups attached to the ligand backbone (Figure 1 and Scheme 2). Such derivatization of photochromic units will allow for their integration inside the rigid core of a porous framework, where spiroopyran photoisomerization could occur within the pore aperture. With this in mind, we prepared 1',3',3'-trimethyl-6-nitro-4',7'-di(pyridin-4-yl)spiro[chromene-2,2'-indoline] (TNDS, Scheme S1), and 1',1''',3',3',3''',3''''-hexamethyl-6,6''-dinitro-4',4'' di(pyridin-4-yl)-7',7''-bispiro[chromene-2,2'-indoline] (HDDB, Scheme S2) via a multistep synthetic procedure as shown in Scheme 2 (six steps for TNDS and seven steps for HDDB, Schemes S1 and S2, respectively). These linkers with one- and two-photoresponsive moieties on one backbone can be also used as a model compound to probe the influence of steric hindrance on spiroopyran isomerization.

All the prepared photochromic linkers and their precursors underwent comprehensive analysis by ¹H and ¹³C NMR, FTIR spectroscopies, single-crystal X-ray diffraction, and mass spectrometry. Detailed description can be found in the Supporting Information (SI) or the experimental section below (Figures S1–S6). The compound, HDDB (Schemes 2 and S2), containing two spiroopyran groups attached to the linker skeleton, is of a particular interest to study the enantiomerization process of spiroopyran units due to resolvable diastereoisomers. As it was previously shown on the example of its precursor,⁹¹ the HDDB linker can exist in three unique diastereoisomers: HDDB_{in-in}, HDDB_{in-out}, and HDDB_{out-out} (Figures 1 and S5). We studied the thermal equilibration process of HDDB in solution to estimate the effect of steric

Scheme 2. Reaction scheme for the synthesis of TNDS (black) and HDDB (grey)^a



^a i) Cu powder, DMF, 120 °C 4 h; ii) SnCl₂, HCl, EtOH, reflux 12 h; iii) NaNO₂, HCl, 0 °C 1 h / CO(NH₂)₂, 0 °C 10 min / SnCl₂, 0 °C, 4 h; iv) 3-methyl-2-butanone, reflux 3 h / H₂SO₄, EtOH, reflux 3 h; v) Et₂O, hexanes, methyl trifluoromethanesulfonate, room temperature, 8 h; vi) 2-hydroxy-5-nitrobenzaldehyde, EtOH, piperidine, reflux 8 h; vii) pyridine-4-boronic acid, PdCl₂(PPh₃)₂, CuCl, Na₂CO₃, DMF, 120 °C, 48 h.⁹¹⁻⁹³

hindrance of spiropyran groups on the possibility of isomerization.

The thermal equilibration of the system was studied using a similar procedure utilized by Klajn and co-workers.⁹⁴ A thermal equilibration process between the three isomers, HDDB_{in-in}, HDDB_{in-out}, and HDDB_{out-out} was represented as a cyclic reversible reaction involving three components with six first-order reactions described by six rate constants (where k = rate constant, C = concentration).

$$\frac{\partial C_{in-in}}{\partial t} = -k_1 C_{in-in} - k_3 C_{in-in} + k_1 C_{in-out} + k_3 C_{out-out}$$

$$\frac{\partial C_{in-out}}{\partial t} = -k_1 C_{in-out} - k_2 C_{in-out} + k_1 C_{in-in} + k_2 C_{out-out}$$

$$\frac{\partial C_{out-out}}{\partial t} = -k_3 C_{in} C_{out-out} - k_2 C_{out-out} + k_3 C_{in-in} + k_2 C_{in-out}$$

To reduce the number of unknown variables, the steady state⁹⁵ was described with following equations:

$$k_1 = k_1(C_{in-in, eq}/C_{in-out, eq})$$

$$k_2 = k_2(C_{in-out, eq}/C_{out-out, eq})$$

$$k_3 = k_3(C_{out-out, eq}/C_{in-in, eq})$$

To be able to monitor thermal isomerization process, we isolated two pure diastereoisomers HDDB_{in-in} and HDDB_{in-out} (see the SI) to track changes of chemical shifts in the NMR spectra for *N*-bound methyl group protons (Scheme 2 and Figure 2), which allow to distinguish between three diastereoisomers. In order to estimate equilibration kinetics between diastereoisomers in solution, HDDB_{in-in} was dissolved in dichloromethane-*d*₂, and its spectra were monitored by ¹H NMR spectroscopy. As shown in Figure 2, the equilibration between the three isomers was reached after three days. We solved the rate equations numerically (see the SI for more details) and obtained six rate constants ($k_1 = 0.214$, $k_1 = 0.122$, $k_2 = 0.228$, $k_2 = 0.402$, $k_3 = 0.481$, $k_3 = 0.481$),

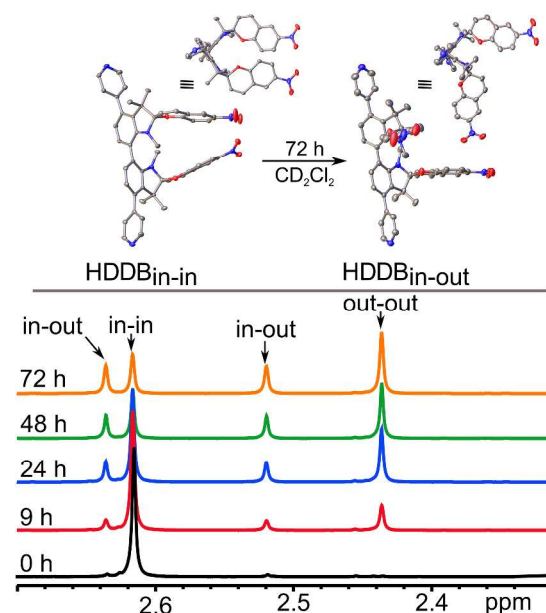


Figure 2. (top) Single crystal X-ray structures of HDDB_{in-in} and HDDB_{in-out}. Two orientations of each diastereoisomer are shown. Displacement ellipsoids drawn at the 60% probability level. Gray, blue, and red spheres represent C, N, and O atoms, respectively. (bottom) A region of the ¹H NMR spectra for thermal equilibration of HDDB_{in-in} to HDDB_{in-out} and HDDB_{out-out} in CD₂Cl₂ is shown at $t = 0, 9, 24, 48,$ and 72 h. The full spectra for the HDDB_{in-in} conversion are shown in Figure S22.

which were used to model the concentration profiles. A good agreement was achieved between the experimental and calculated results. The obtained rate constant values were similar to those of the HDDB precursor (VII', Scheme S2). Therefore, we can hypothesize that the extension of ligand backbone containing spiropyran moieties with pyridyl group does not significantly affect isomerization rates.

Synthesis of Photoresponsive 1, 2, 3, 3', and 4 MOFs

The prepared linkers were used for coordinative immobilization inside the porous scaffolds. We used two distinct approaches for linker incorporation. One approach relies on coordination of linkers containing pyridyl groups to unsaturated metal sites of a framework. Three photochromic ligands TNDS, HDDB, and BPMTC (Figure 3) contain terminal pyridyl groups, which make them suitable for incorporation between two-dimensional (2D) MOF layers. For instance, BPMTC, has been previously utilized as pillars in a MOF, in which 2D layers consist of a tetracarboxylate linker, DBTD⁴⁻

(H₄DBTD = 3',6'-dibromo-4',5'-bis(4-carboxyphenyl)-1[1,1':2',1''-tetraphenyl]-4,4''-dicarboxylic acid, Figure 3).²⁹ We anticipated that our novel spiropyran pillars could also bind axially to the zinc paddlewheel secondary building units (SBUs). Indeed, integration of TNDS and HDDB were performed between 2D layers, consisting of DBTD⁴⁻ connected by Zn₂(O₂C)₄, and resulted in formation of Zn₂(DBTD)(TNDS) (**1**), Zn₂(DBTD)(HDDB) (**2**), and Zn₂(DBTD)(BPMTC) (**3**), Figures 3, S7–S14, see experimental details in the SI).

As discussed above, the structures consist of stacked layers of DBTD⁴⁻ connected in the equatorial planes of planar zinc paddlewheel SBUs (Figure 3). Both **1** and **2** consist of a

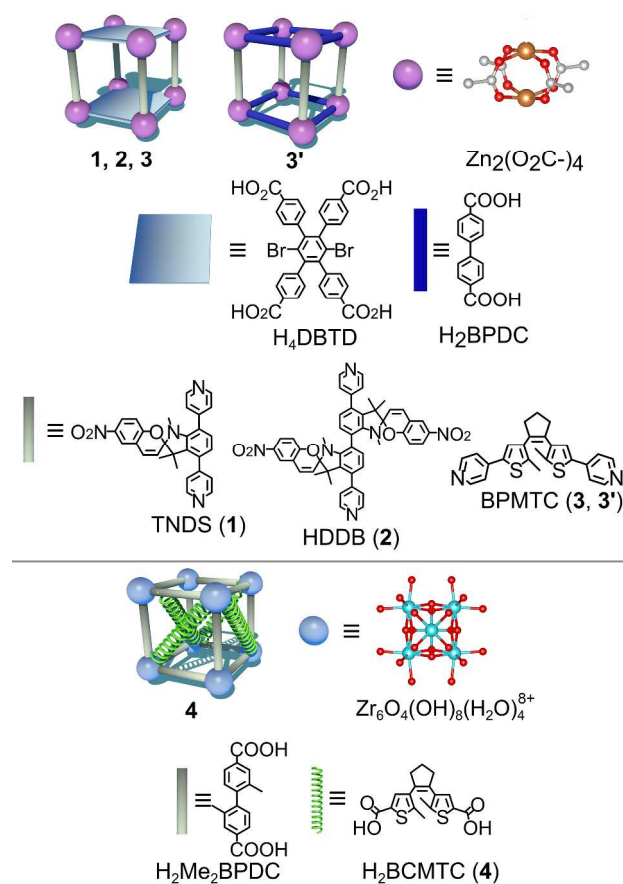


Figure 3. (top) The TNDS, HDDB, and BPMTc linkers were used to synthesize **1**, **2**, and **3** (**3'**), respectively, in the presence of H_4DBTD (H_2BPDC). (bottom) The linker, H_2BCMTc , was installed as a capping linker into an existing MOF framework, $Zr_6(Me_2BPDC)_4$,⁷⁷ to make **4**. Orange, red, teal, and gray spheres correspond to zinc, oxygen, zirconium, and carbon atoms, respectively.

pillar backbone with three and four six-membered rings, respectively, which are anchored to the axial positions of the SBUs with two-fold disorder (for more details see the crystallographic section of the SI, Table S3). The bulk samples of **1** and **2** were also characterized using PXRD, and the acquired data are in agreement with their simulated patterns (Figure 4). The 1H NMR spectroscopic studies of digested **1** (i.e., destroyed in the presence of hydrochloric acid) also confirm the presence of the photochromic pillars (Figure S9). The $^{13}C\{^1H\}$ CP-MAS NMR spectroscopic analysis confirmed integration of photochromic moieties in **2** (Figure S12). The FTIR spectra of **1** and **2** are shown in Figures S8 and S11, respectively.

MOF **3** contains the BPMTc linker coordinatively anchored between the axial zinc paddlewheel SBUs and the 2D layers of $DBTD^{4-}$, as it was previously reported (Figure 3).²⁹ The powder pattern of the bulk sample of **3** was in good agreement with the simulated pattern (Figure S13). The 1H NMR spectrum of the digested sample shows the presence of both BPMTc and H_4DBTD (Figure S14). The structure **3'** consisting of the same BPMTc linker integrated between 2D sheets composed of the Zn-based paddle-wheel connected by $BPDC^{2-}$ linkers (Table S3, Figures S15–S17). Single-

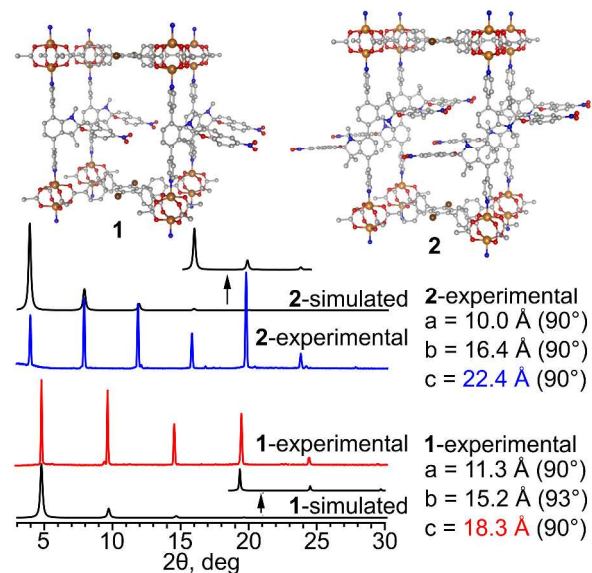


Figure 4. (top) Single-crystal structures of **1** and **2** with simulated spiropyran moiety located in the pores. (bottom) The simulated and experimental PXRD patterns of MOFs **1** (red) and **2** (blue). The colored text shows the increase of interlayer distance for each MOF, which is in agreement with the sizes of the installed photochromic linkers.

crystal X-ray diffraction showed the presence of two-fold interpenetrated frameworks (Figure S15 and Table S3).

In the case of **4**, we applied a different method for coordinative immobilization of H_2BCMTc inside the porous scaffold. We integrated a photochromic compound as a capping linker in an already synthesized framework using a previously developed synthetic methodology.⁹⁶ For that, we used a Zr-based framework, $Zr_6(Me_2BPDC)_4$,⁷⁷ consisting of 2,2'-dimethylbiphenyl-4,4'-dicarboxylate, Me_2BPDC^{2-} , linkers coordinated to $Zr_6O_4(OH)_8(H_2O)_4^{8+}$ metal nodes (Figure 3). The H_2BCMTc integration occurred through replacement of the terminal OH^- and H_2O groups in the SBU. The schematic representation of such installation is shown in Figure 3 and more details about suitable linkers for such coordination as well as calculation of the appropriate linker size could be found elsewhere.⁹⁷ However, it is important to note that $Zr_6(Me_2BPDC)_4$ is flexible enough to accommodate structural changes associated with capping linker insertion. The powder pattern of prepared $Zr_6(Me_2BPDC)_4$ was also in good agreement with the simulated pattern,⁷⁷ and framework crystallinity was retained after incorporation of $BCMTc^{2-}$ (Figure S18). To remove any traces of residual (non-coordinated) linkers, we applied an extensive washing procedure using a Soxhlet apparatus. After that, the installation of $BCMTc^{2-}$ into **4** was confirmed by 1H NMR spectroscopy of digested **4** (Figure S19). In combination with experimental spectroscopic studies, the geometrical constraints placed by the linker size and pocket dimension of the framework suggest that the capping linker can occupy both axial and equatorial positions of Zr-nodes, ca. 50% occupancy of available sites.

Photophysics of Photochromic Compounds

The photoswitching behavior of photochromic molecules with spiropyran and diarylethene cores are vastly distinct mainly due to the nature of structural changes associated with photoinduced isomerization. The expansion of the photoswitch from the spiropyran form to the merocyanine form is accom-

panied with significant structural changes, and therefore, can severely impact the photoisomerization rate.^{4,98–100} In general, spiropyran derivatives consist of two moieties: indoline and chromene linked together through a single sp^3 “spiro” chiral carbon. Once the photoswitch is irradiated with UV light ($\lambda_{\text{ex}} < 400$ nm), the photoswitch undergoes a cyclization reaction and generates a highly colored, zwitterionic form (merocyanine), shown in Figure 1.⁸⁵

Diarylethene photoswitches also have two isomeric forms, colorless (“open”) and colored (“closed”, Figure 1). The colorless “open” form of diarylethene can be irradiated with UV light, which causes formation of a bond between the two heterocyclic thiophene moieties, generating the colored diarylethene form (Figure 1).⁸⁰ However, the diarylethene photoswitch, unlike spiropyran, is thermally stable in either form and does not undergo such a drastic structural change during isomerization. In fact, relatively little movement of diarylethene “arms” within the same plane is necessary to achieve rapid photoisomerization, particularly in the solid state.

To probe photoisomerization kinetics of the prepared spiropyran and diarylethene derivatives for the first time, we performed photophysical measurements in solution and in the solid state. For solution studies, a 3 mM solution of the photoswitch was loaded into a 8 mm \times 1 mm front-facing quartz sample cell. For solid-state studies, 4 μ mol of photoswitch was mixed with 100 mg of potassium bromide, which was then pressed into the same 8-mm sample cell.

Spiropyran Derivatives in the Solid State, Solution, and Coordinatively Immobilized in Scaffolds 1 and 2

The photochromic cycloreversion kinetics of both the TNDS and HDDB linker were investigated in the solid state, solution, as well as coordinatively inside scaffolds (Figures 3, 4, and S7–S12). Figure 5 shows photoisomerization of TNDS in the solid state and solution with an excitation wavelength of 365 nm. As expected, the TNDS powder was not fully reversible due to the necessity of significant structural changes required for the photoisomerization process. As a result, the TNDS derivative displayed limited photoconversion to the colorless form in the solid state, whereas in solution, complete photoinduced reversion was successfully achieved.

The photophysical studies of TNDS in *N,N*-dimethylformamide (DMF) showed a linear correlation between $\ln(A)$ versus time of irradiation, which is in line with the data previously reported for other spiropyran-derivatives in solution.^{90,101–103} The rate constant, k , was found to be 0.12 s^{-1} . Cycloreversion plots and experimentally determined rates are shown in Figure 6 and Table 1, respectively.

In comparison with TNDS, HDDB also showed limited photoisomerization in the solid state, while demonstrating 100% photoconversion in solution. However, measurements of photoisomerization rates in solution were complicated by the presence of three isomers, HDDB_{in-in}, HDDB_{in-out}, and HDDB_{out-out} (Figure 1), each of which possess a different photoisomerization rate. For the isolated HDDB_{in-in} isomer, k , was found to be 0.20 s^{-1} in DMF, which decreases

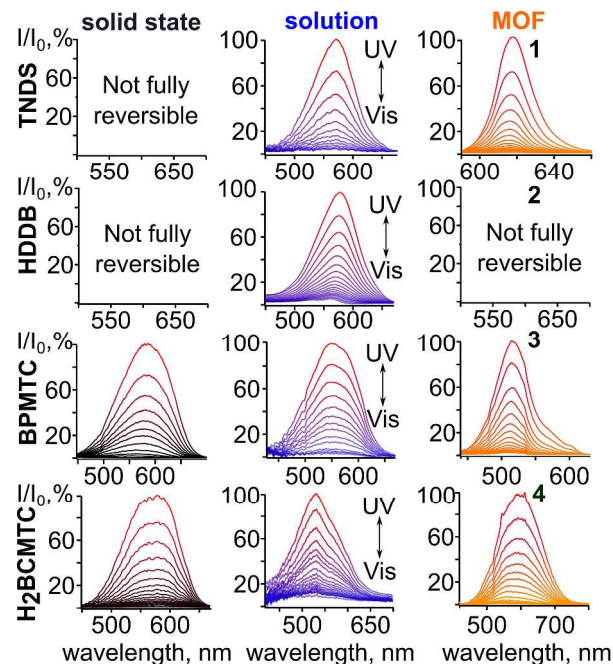


Figure 5. Normalized absorption plots of TNDS, HDDB, BPMTc, H₂BCMTC in the solid state, solution, and coordinatively immobilized inside MOF upon irradiation with UV and visible light.

up to 0.06 s^{-1} during conversion of HDDB_{in-in} to HDDB_{in-out} and HDDB_{out-out}. Coordinative immobilization of TNDS and formation of **1** significantly affects its photophysics. Indeed, once TNDS was integrated into a rigid scaffold, it demonstrated solution-like photoisomerization behavior, even in the solid state. Integrated TNDS (**1**) showed a 100% conversion from merocyanine to spiropyran with a rate of 0.16 s^{-1} (Figures 5 and 7, Table 1). Therefore, a framework provides a pathway for photoswitch isomerization in the solid state through the spatial separation of photochromic linkers in contrast to the close packing observed for free ligand in the solid state.

Based on the results observed for **1**, we integrated the bulkier HDDB inside the rigid scaffold resulting in preparation of **2**. However, HDDB does not exhibit photophysical behavior similar to TNDS. In contrast, HDDB exhibits limited photoisomerization more typical for the solid state, rather than that in solution. Such difference between integrated HDDB and TNDS could be attributed to the presence of two photoswitchable moieties and their close proximity in a framework, which impede the complete cycloreversion process. Thus, comparison of integrated TNDS versus coordinatively embedded HDDB possessing the same photoresponsive moieties, but dissimilar in their amount (**1** vs **2**, respectively), allowed us to demonstrate the crucial role of steric hindrance in the photoisomerization process.

Diarylethene Derivatives in the Solid State, Solution, and Coordinatively Immobilized in 3, 3', and 4 Scaffolds

In the case of diarylethene photoswitches, we found that both BPMTc and H₂BCMTC were fully reversible in the solid state and solution (λ_{ex} (cyclization) = 365 nm, λ_{ex} (cycloreversion) \geq 400 nm, Figure 1). In solution, the rate constants, k , for the BPMTc cycloreversion reaction varied in a narrow range

Table 1. The rate constants of cycloreversion process (k , s^{-1})

1) of TNDS, HDDB, BPMTC, and H₂BCMTC, in the solid-state, solution, and coordinatively immobilized in a MOF.

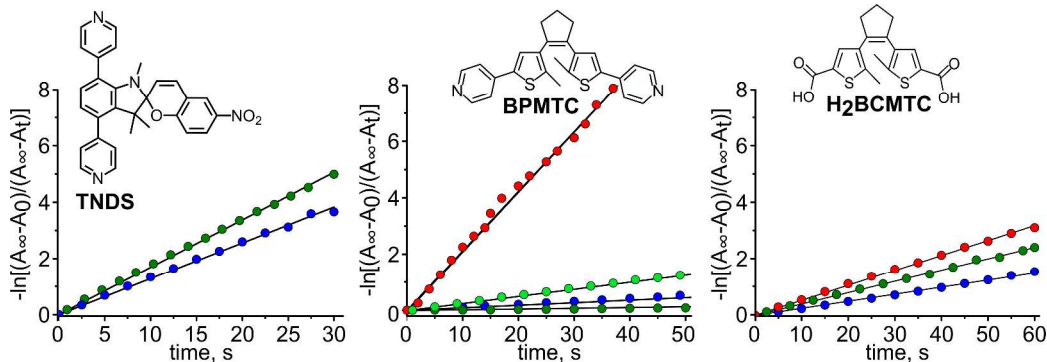
	solid state	solution	MOF
TNDS	n/a ^a	1.2×10^{-1} ^b	1.6×10^{-1} (1)
HDDB	n/a ^a	$(6.0-20) \times 10^{-2}$ ^b	n/a (2) ^a
BPMTC	2.0×10^{-1}	1.0×10^{-2} ^b	2.8×10^{-3} (3) 2.0×10^{-2} (3')
H₂BCMTC	4.8×10^{-2}	2.6×10^{-2} ^c	4.1×10^{-2} (4)

^a Photoisomerization was not fully reversible

^b $C = 3$ mM in DMF

^c $C = 3$ mM in MeOH

from 0.01 to 0.03 s⁻¹ (Figures 5–7, Tables 1 and 2). The obtained k values for BPMTC are in line with literature data reported for other diarylethene derivatives and support the previous hypothesis that solvent polarity does not exhibit a significant effect on the cycloreversion process due to irrelevance of ring-opening process to changes in a molecular conformation.^{79,104–108} The photoisomerization rate for H₂BCMTC in methanol (2.6×10^{-2} s⁻¹) was also comparable with the rate of BPMTC in the same solvent (1.8×10^{-2} s⁻¹, Figure 6, Tables 1 and 2). However, in contrast to spiropyran derivatives, diarylethene photoswitches underwent fast cycloreversion in the solid state, which could be explained by the accommodation of strain energy generated by the geometrical structure change during the cyclization reaction as well as the low activation energy of ring-opening process.^{105–107} For instance, photoinduced isomerization of BPMTC occurs with a rate of $k = 0.20$ s⁻¹. However, this tendency was not observed for coordinatively immobilized BPMTC inside a rigid framework. In **3**, where the BPMTC linker is coordinatively immobilized as a pillar between DBTD⁴⁻-containing layers (Figure 3), the recovery of the open-form isomer was found to be 0.0028 s⁻¹, which is ~70 times slower in comparison with the “free” compound in the solid state. Such a drastic rate decrease could be associated with the fact that the BPMTC pyridyl arms are tethered between the two-dimensional layers of DBTD⁴⁻, which impede the possibility of pillar photoisomerization since photoinduced transformations should occur through the linker skeleton. By changing framework topology, we were able to enhance the photoisomerization rate by almost four times. Thus, BPMTC in framework **3'**, connected to the skeleton of Zn-BPDC units, consisting of more flexible dicarboxylic units, BPDC²⁻, photoisomerizes with the rate $k = 0.01$ s⁻¹. Remarkably, the obtained k value for **3'** correlates with behavior of the linker in solution (Tables 1 and 2, Figure S17) and could be attributed



to a high degree of framework flexibility in **3'** in comparison with **3**. Notably, both **3** and **3'** frameworks were able to accommodate structural changes associated with the photoisomerization process of BPMTC coordinatively immobilized between metal nodes, which was confirmed by PXRD. Thus, a rigid framework allowed us to tune the photoisomerization rate mimicking solution or solid-state behavior as a function of its topology.

In the case of H₂BCMTC, the rate constant in the solid state was found to be 4.8×10^{-2} s⁻¹, which is four times slower in comparison with BPMTC (Figures 5 and 7, Table 1) as well as other diarylethene derivatives.^{79,104–108} Such difference could be explained by the fact that H₂BCMTC could result in formation of a “hydrogen-bonding” framework with behavior similar to a MOF matrix (Figure S23). We hypothesize that hydrogen-bonding interactions in the solid state could restrict molecular dynamics in the similar fashion as a MOF and potentially be a reason for the similar rate constants (4.1×10^{-2} s⁻² (**4**) and 4.8×10^{-2} s⁻¹ (solid state, Table 1).

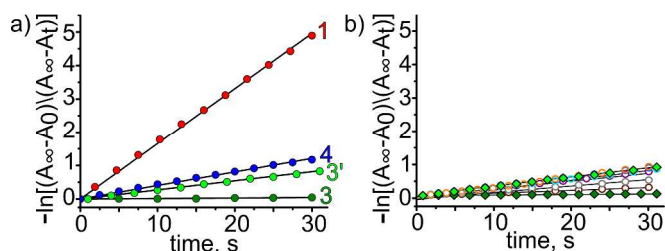


Figure 6. a) The cycloreversion kinetics of photochromic MOFs upon irradiation with visible light. b) The cycloreversion kinetics plots for BPMTC linker in solution (circles, brown - ethanol, grey - methanol, purple - acetonitrile, light blue – tetrahydrofuran, blue – toluene, and orange – chloroform) and coordinatively immobilized inside MOFs **3** (dark green diamonds) and **3'** (light green diamonds).

Figure 7. The cycloreversion kinetics of TNDS, BPMTc, and H₂BCMTC as a solid (red), solution (blue: TNDS and BPMTc in DMF and H₂BPMTc in methanol; the solvent was chosen according to solubility and photochromic behavior), and immobilized in a MOF (green) upon irradiation with visible light.

To summarize this subsection, we showed the effect of a rigid scaffold on photoisomerization kinetics for two distinct classes of photochromic molecules. Based on the comparison of spiro- and diarylethene-based linkers possessing different photoisomerization pathways, we promoted photoinduced isomerization of spiro-derivatives in the solid state through their integration inside a porous matrix. Moreover, coordinatively immobilized spiro-derivatives can mimic solution-like photophysical behavior. However, steric hindrance still could impede photoisomerization dynamics as it was shown on the example of the photochromic linker possessing two spiro- moieties located in close proximity to each other. On the example of diarylethene-based frameworks with different topologies and structural flexibilities, we showed the possibility to tune and control the photoisomerization rate of incorporated photochromic linkers with a level of control, which cannot be achieved in the solid state or solution. To the best of our knowledge, the presented studies are the first example of extensive photophysical studies demonstrating tunability of photoisomerization rates within two orders of magnitude for the same organic linker (Figure 6). We hypothesize that such drastic difference in behavior could be potentially tuned as a function of framework topology, which provides a pathway for development of new “smart” photo-switchable materials with a controllable photoresponsive.

Photochromic Compounds to Map Changes in Material Properties

The concept of photoisomerization inside a confined environment discussed above could be potentially translated towards mapping of changes in a profile of a material. We tested the hypothesis that prepared photochromic porous scaffolds, overcoming steric hindrance for photoisomerization processes, can be utilized as a marker for material degradation. The advantage of a porous framework is that it promoted photoisomerization under irradiation (or daylight exposure), and the changes in the photophysical profile of a material became “invisible” due to a relatively rapid photoisomerization when the scaffold is intact, i.e., its integrity is maintained.

In our studies, we used the TNDS-containing MOF (**1**), which was mixed with potassium bromide, leading to formation of the slightly colored homogeneous mixture (Figure 8 and S24). After deposition of the obtained mixture on filter paper, nitrogen gas was bubbled through a 6 M HCl solution. Notably, exposure to just nitrogen did not lead to any surface changes. Hydrochloric acid vapors were released through a narrow tip (*i.d.* = 4 mm) to localize their effect. As shown in Figure 8, such treatment resulted in local framework degradation, which is accompanied with linker release, i.e., formation of non-coordinated photochromic TNDS. Surface changes were monitored by photoluminescence spectroscopy while structural ones by PXRD. Figure 8 demonstrates that before acid vapor exposure, the emission profile has a maximum of $\lambda_{\text{max}} = 680 \text{ nm}$ ($\lambda_{\text{ex}} = 350 \text{ nm}$) but framework degradation causes a hypsochromic shift of more than 100 nm, and therefore the emission maximum became similar to that of a “free” photochromic linker. These drastic changes in emission (from

purple to green) allowed detection of scaffold degradation by the naked eye. Moreover, these changes were local, i.e., occurred only at the exposed area. As a control experiment, the non-coordinated linker, TNDS, was exposed to HCl vapors under

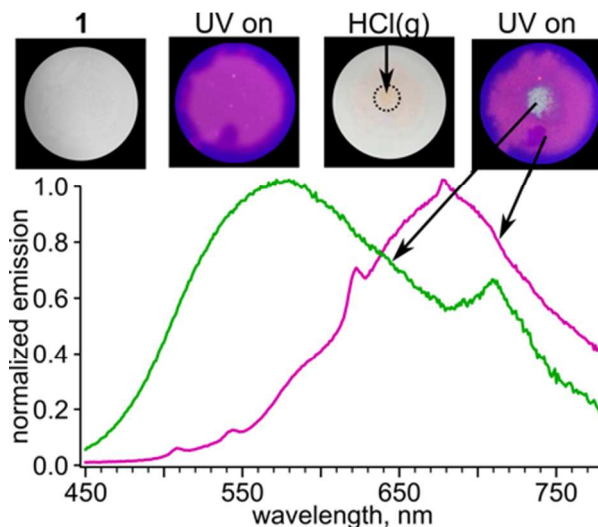


Figure 8. (top) The surface of **1** was subjected to HCl vapors and shows evidence of MOF degradation at the point of contact. (bottom) The fluorescence spectra of **1** before (purple) and after (green) exposure to HCl vapors.

similar conditions (Figure S20). In that case, we observed similar emission with $\lambda_{\text{max}} = 550 \text{ nm}$ ($\lambda_{\text{ex}} = 345 \text{ nm}$) to that of the “exposed” framework. The same protonation of TNDS was observed in solution by bubbling HCl vapors (Figure S21). Furthermore, due to framework degradation (monitored by PXRD studies), the “released” photochromic TNDS highlighted the corroded areas permanently, which provided a pathway to use such changes as a good indicator for necessary material treatment or replacement. To summarize, the presented concept could be applied towards invasive monitoring of material surfaces with a good spatial resolution. These studies could potentially provide an avenue to monitor material aging or structural deterioration, which are key points for a number of industrial processes or applications including tests of aircraft reliability or steel corrosion.

CONCLUSION

The presented studies focus on photoisomerization kinetics of two distinct classes of photochromic derivatives with spiro- and diarylethene cores in the solid state, solution, and coordinatively immobilized inside the rigid scaffold. To study such dependence as well as the possible effect of steric hindrance, we prepared two novel spiro- compounds, TNDS and HDDB with one and two photoswitching moieties, which resulted in preparation of the first examples of MOFs (**1** and **2**) with spiro- moieties embedded as a part of the organic linker. Due to the presence of different HDDB isomers (HDDB_{in-in}, HDDB_{in-out}, and HDDB_{out-out}), we were also able to study thermal equilibration process of HDDB in solution to estimate the effect of steric hindrance of spiro- groups on isomerization.

For the first time, through utilization of five distinct frameworks (**1**, **2**, **3**, **3'** and **4**), we also showed that (i) the solid-state spiroopyran metal-organic materials with capability of reversible photoinduced isomerization could be prepared; (ii) a photochromic linker could be integrated not only as pillars but as well as postsynthetically-installed capping linkers; (iii) the photoisomerization rate could be tuned as a function of framework structure; (iv) coordinatively immobilized spiroopyran derivatives inside a MOF could possess a high isomerization rate mimicking solution behavior; and (v) the acquired fundamental principles could be translated towards mapping changes in material properties to develop stimuli-responsive markers.

To conclude, the presented studies not only address some aspects of photophysics of photochromic compounds integrated in a confined environment, but also provide a pathway for development of a new generation of photoactive materials.

EXPERIMENTAL SECTION

Materials. Zinc(II) nitrate, hexahydrate (technical grade, Ward's Science), tin(II) chloride, anhydrous (98%, Beantown Chemicals), copper(I) chloride, anhydrous (97%, Strem Chemicals), bis(triphenylphosphine)palladium(II) dichloride (96%, Oakwood Chemical), copper powder (99.9%, Alfa Aesar), sodium carbonate (ACS grade, Ameresco), magnesium sulfate, anhydrous (USP, Chem-Impex, International Inc.), sodium sulfate, anhydrous (99.5%, Oakwood Chemical), sodium hydroxide (ACS, Oakwood Chemical), 2,5-dibromonitrobenzene (99%, Oakwood Chemical), sodium nitrite (98%, Oakwood Chemical), 3-methyl-2-butanone (98%, Beantown Chemicals), methyl trifluoromethanesulfonate (97%, Matrix Scientific), 2-hydroxy-5-nitrobenzaldehyde (98%, Oakwood Chemical), pyridine-4-boronic acid (95%, Matrix Scientific), hexabromobenzene (>99%, TCI America), *p*-tolylmagnesium bromide (0.5 M in diethyl ether, Acros Organics), hydrochloric acid (ACS, Fisher Chemical), sulfuric acid (ACS grade, Fisher Chemical), nitric acid (ACS reagent, Sigma-Aldrich), fluoboric acid (48%, Oakwood Chemical), ethanol (200 proof, Decon Laboratories, Inc), methanol (ACS grade, Fisher Scientific), methylene chloride (99.9%, Fisher Chemical), acetone (ACS grade, Sigma Aldrich), ethyl acetate (99.9%, Fisher Chemical), chloroform (99.9%, Fisher Chemical), diethyl ether (ACS grade, J. T. Baker® Chemicals), hexanes (ACS, BDH), *N,N*-dimethylformamide (ACS grade, Oakwood Chemical), piperidine (99%, Sigma-Aldrich), carbon tetrachloride (99.9%, Sigma-Aldrich), bromine (99.8%, Acros-Organic), tetrahydrofuran (HPLC grade, Beantown Chemicals), chloroform-*d* (Cambridge Isotopes), acetone-*d*₆ (Cambridge Isotopes), methylene chloride-*d*₂ (Cambridge Isotopes), dimethyl sulfoxide-*d*₆ (Cambridge Isotopes) were used as received.

The compounds 2,5-dibromoaniline (**II**, Scheme S1),⁹² (2,5-dibromophenyl)hydrazine (**III**, Scheme S1),⁹³ 4,7-dibromo-2,3,3-trimethyl-3*H*-indole (**IV**, Scheme S1),⁹³ 4,4'-dibromo-2,2'-dinitro-1,1'-biphenyl (**II'**, Scheme S2),⁹¹ 4,4'-dibromo-[1,1'-biphenyl]-2,2'-diamine (**III'**, Scheme S2),⁹¹ (4,4'-dibromo-[1,1'-biphenyl]-2,2'-diyl)bis(hydrazine) (**IV'**, Scheme S2),⁹¹ 4,4'-dibromo-2,2',3,3,3',3'-hexamethyl-3*H*,3'*H*,7,7'-biindole (**V'**, Scheme S2),⁹¹ 3',6'-dibromo-4',5'-bis(4-carboxyphenyl)-1[1,1':2',1''-tetraphenyl]-4,4''-dicarboxylic acid (H₄DBTD, Figure 3),¹⁰⁹ 1,2-bis(2-methyl-5-(pyridin-4-yl)thiophen-3-yl)cyclopent-1-ene (BPMTC, Figures 1 and 3),⁸² 4,4'-(cyclopent-1-ene-1,2-diyl)bis(5-methylthiophene-2-carboxylic acid) (H₂BCMTC, Figures 1 and 3),⁸³ 2,2'-dimethylbiphenyl-4,4'-dicarboxylic acid (H₂Me₂BPDC),¹¹⁰ and Zr₆(Me₂BPDC)₄⁷⁷ were prepared according to the reported procedures.

Preparation of [4,7-dibromo-1,2,3,3-tetramethyl-3*H*-indol-1-ium][trifluoromethanesulfonate] ([C₁₂H₁₄Br₂N]⁺ [CF₃O₃S]⁻, **V**, Scheme S1).

Compound **V** (Scheme S1) was prepared based on a modified literature procedure.⁹¹ Methyl trifluoromethanesulfonate (4.13 g, 25.2 mmol) was added to synthesized **IV** (Scheme S1) (2.00 g, 6.31 mmol) in 120 mL of diethyl ether and 80 mL of hexanes. After the resulted mixture was stirred vigorously for 8 hours at room temperature, a pale pink powder was collected by filtration and washed with diethyl ether (3 × 10 mL). After drying under vacuum, **V** (Scheme S1) (2.70 g, 5.61 mmol) was isolated in 89% yield and used without further purification.

Preparation of 4',7'-dibromo-1',3',3'-trimethyl-6-nitrospiro[chromene-2,2'-indoline] (C₁₉H₁₆Br₂N₂O₃, **VI**, Scheme S1).

Under a nitrogen atmosphere, piperidine (1.41 g, 16.6 mmol) was added to a solution of **V** (2.00 g, 4.15 mmol, Scheme S1) and 2-hydroxy-5-nitrobenzaldehyde (1.25 g, 7.47 mmol) in 80 mL of ethanol and heated at reflux for 8 h. After cooling to 0 °C, the resulting light-yellow precipitate was filtered and washed with cold ethanol. After drying under vacuum, **VI** (0.971 g, 2.02 mmol, Scheme S1) was isolated in 48% yield. Crystals of **VI** (Scheme S1) were obtained upon cooling of the crude reaction mixture in ethanol at 0 °C over several days. The detailed description for the crystallographic data collection and refinement details are given in the SI (Table S1). The determined structure of **VI** (Scheme S1) is shown in Figure S1. ¹H NMR (acetone-*d*₆, 300 MHz): δ = 1.27 (3H, s), 1.49 (3H, s), 3.17 (3H, s), 6.00-6.04 (1H, d, *J* = 10.4 Hz), 6.92-6.95 (1H, d, *J* = 8.55 Hz), 6.96-6.99 (1H, d, *J* = 9.00), 7.26-7.29 (1H, d, *J* = 8.62 Hz), 7.30-7.33 (1H, d, *J* = 10.4 Hz), 8.09-8.13 (1H, dd, *J* = 2.83, 8.96 Hz) ppm (Figure S2). ¹³C NMR (acetone-*d*₆, 400 MHz): δ = 20.61, 22.46, 32.91, 54.59, 101.15, 108.00, 116.27, 118.15, 119.48, 121.36, 123.81, 126.69, 126.75, 130.59, 135.93, 136.86, 142.31, 147.37, 160.18 ppm (Figure S2). FTIR (neat, cm⁻¹): 3076, 2968, 2934, 2868, 2545, 2162, 2041, 1980, 1910, 1736, 1654, 1614, 1577, 1510, 1478, 1466, 1443, 1396, 1379, 1361, 1331, 1272, 1255, 1228, 1175, 1145, 1127, 1088, 1061, 1017, 955, 927, 915, 904, 877, 834, 811, 792, 771, 745, 717, 703, 666. HRMS (ESI, *m/z*) calculated for C₁₉H₁₆Br₂N₂O₃ [M+H]⁺ 478.9601, found 478.9600.

Preparation of 1',3',3'-trimethyl-6-nitro-4',7'-di(pyridin-4-yl)spiro[chromene-2,2'-indoline] (C₂₉H₂₄N₄O₃, **TNDS**, Scheme S1).

Using a Schlenk technique, 25 mL of dry DMF was transferred into a flask containing **VI** (300 mg, 0.624 mmol, Scheme S1), Na₂CO₃ (240 mg, 2.26 mmol), PdCl₂(PPh₃)₂ (88.0 mg, 0.125 mmol), CuCl (134 mg, 1.35 mmol), and pyridine-4-boronic acid (460 mg, 3.74 mmol). The obtained mixture was stirred for three days at 120 °C. After cooling to room temperature, the reaction mixture was transferred into a 250-mL separatory funnel, following dilution with deionized water (75 mL). The product was then extracted with ethyl acetate (3 × 50 mL). The organic layers were combined and washed with brine (50 mL), dried over sodium sulfate, followed by filtration and solvent removal under vacuum. The resulting red/brown oil underwent several recrystallizations in ethyl acetate and hexanes. The obtained orange powder was dissolved in ethyl acetate (20 mL) and hexanes (30 mL), and the solvent was removed under vacuum until a suspension formed. The suspension was filtered to collect a light-yellow powder. After drying on vacuum, **TNDS** (44.0 mg, 93.8 μmol) was isolated in 17% yield. Single crystals of **TNDS** were obtained by slow evaporation of saturated acetone solution at 0 °C. The detailed description for the crystallographic data collection and refinement details are given in the SI (Table S2).

The X-ray structure of TNDS is shown in Figure S3. ^1H NMR (acetone- d_6 , 400 MHz): δ = 0.81 (3H, s), 1.33 (3H, s), 2.43 (3H, s), 6.00–6.03 (1H, d, J = 10.5 Hz), 6.69–6.71 (1H, d, J = 7.9 Hz), 6.85–6.88 (1H, d, J = 9.0 Hz), 7.12–7.14 (1H, d, J = 7.9 Hz), 7.18–7.22 (1H, d, J = 10.6 Hz), 7.39–7.45 (1H, m), 8.01–8.05 (1H, dd, J = 2.8 Hz and 9.0 Hz), 8.08 (1H, d, J = 2.8 Hz), 8.64 (4H, m) ppm (Figure S4). ^{13}C NMR (acetone- d_6 , 400 MHz): δ = 20.61, 22.46, 32.91, 54.59, 101.14, 108.00, 116.27, 118.15, 119.49, 121.36, 123.81, 126.74, 130.59, 135.93, 136.86, 142.31, 147.37, 160.18 ppm (Figure S4). FTIR (neat, cm^{-1}): 3746, 2965, 2344, 2163, 2049, 1981, 1596, 1543, 1522, 1494, 1464, 1438, 1392, 1363, 1337, 1286, 1253, 1216, 1145, 1129, 1072, 1055, 1011, 980, 939, 905, 873, 827, 803, 749, 729, 681 (Figure S8). HRMS (ESI, m/z) calculated for $\text{C}_{29}\text{H}_{24}\text{N}_4\text{O}_3$ $[\text{M}+\text{H}]^+$ 477.1918, found 477.1921.

Preparation of [4,4'-dibromo-1,1',2,2',3,3',3',3'-octamethyl-3H,3'H-[7,7'-biindole]-1,1'-diium]bis-[trifluoromethanesulfonate] ($[\text{C}_{24}\text{H}_{28}\text{Br}_2\text{N}_2]^{2+} [(\text{CF}_3\text{O}_3\text{S})_2]^{2-}$, **VI'**, Scheme S2).

Compound **VI'** (Scheme S2) was prepared based on a modified literature procedure.⁹¹ Methyl trifluoromethanesulfonate (1.50 g, 10.1 mmol) was added to synthesized **V'** (Scheme S2) (1.00 g, 2.11 mmol) in 90 mL of diethyl ether and 60 mL of hexanes. After the resulted mixture was stirred vigorously for 8 h at room temperature, a pale pink powder was collected by filtration and washed with diethyl ether (3×10 mL). After drying under vacuum, **VI'** (1.57g, 1.96 mmol, Scheme S2) was isolated in 93% yield and used without further purification.

Preparation of 4',4''-dibromo-1',1''',3',3''',3''''-hexamethyl-6,6''-dinitro-7',7''''-bisp[chromene-2,2'-indoline]

($\text{C}_{38}\text{H}_{32}\text{Br}_2\text{N}_4\text{O}_6$, **VII'**, Scheme S2).

Compound **VII'** (Scheme S2) was prepared based on a modified literature procedure.⁹¹ Using a Schlenk technique, piperidine (713 mg, 8.37 mmol) was added to a solution of **VI'** (Scheme S2) (1.50 g, 1.87 mmol) and 2-hydroxy-5-nitrobenzaldehyde (706 mg, 4.38 mmol) in 60 mL of ethanol and heated at reflux for 8 h. After cooling to 0 °C, the resulting light-yellow precipitate was filtered and washed with cold ethanol. After drying under vacuum, **VII'** (761 mg, 948 μmol , Scheme S2) was isolated in 51% yield. ^1H NMR (acetone- d_6 , 400 MHz): δ = 1.30 (6H, s), 1.43 (6H, s), 2.59 (6H, s), 5.96–5.99 (2H, d, J = 10.4 Hz), 6.34–6.37 (2H, d, J = 9.00 Hz), 6.87–6.90 (2H, d, J = 8.18 Hz), 6.97–7.00 (2H, d, J = 8.25 Hz), 7.24–7.28 (2H, d, J = 10.4 Hz), 7.59–7.54 (2H, dd, J = 2.77 and 9.01), 8.10 (2H, d, J = 2.73 Hz). FTIR (neat, cm^{-1}): 3556, 3076, 2976, 2934, 2873, 2258, 2162, 2040, 1980, 1895, 1654, 1614, 1572, 1513, 1473, 1447, 1435, 1397, 1363, 1336, 1274, 1255, 1232, 1179, 1148, 1126, 1088, 1062, 1022, 1001, 950, 923, 905, 863, 823, 799, 766, 747, 709, 697.

Preparation of 1',1''',3',3''',3''''-hexamethyl-6,6''-dinitro-4',4''''-di(pyridin-4-yl)-7',7''''-bisp[chromene-2,2'-indoline] ($\text{C}_{48}\text{H}_{40}\text{N}_6\text{O}_6$, **HDDDB**, Scheme S2).

Using a Schlenk technique, 20 mL of dry DMF was transferred to a flask containing **VII'** (336 mg, 420 μmol , Scheme S2), Na_2CO_3 (84.0 mg, 793 μmol), $\text{PdCl}_2(\text{PPh}_3)_2$ (47.0 mg, 670 μmol), CuCl (168 mg, 1.69 mmol), and pyridine-4-boronic acid (206 mg, 1.68 mmol). The resulting mixture was stirred for two days at 120 °C. After cooling to room temperature, the reaction mixture was transferred in a 250 mL separatory funnel, following dilution with deionized water (75 mL). The product was then extracted with ethyl acetate (3×50 mL). The organic layers were combined and washed with brine (50 mL), dried over sodium sulfate, followed by filtration and solvent removal under vacuum. The obtained red/brown oil was recrystallized several times using ethyl acetate and hexanes. The resulting orange powder was dissolved in ethyl

acetate (20 mL) and hexanes (30 mL) and the solvent was removed under vacuum until a suspension formed. The suspension was filtered to collect a light-tan powder. After drying on vacuum, **HDDDB** (50.0 mg, 625 μmol) was isolated in 15% yield. In order to obtain crystals of a specific diastereomer of **HDDDB**, it was subjected to preparatory TLC using a 5:95 (v:v) methanol/dichloromethane, in which the product was extracted with acetone followed by slow evaporation of the solvent overnight, and crystals of **HDDDB_{in-in}** were isolated. Single crystals of **HDDB_{in-out}** were obtained from a solution of **HDDDB** in 50:50 (v:v) ethyl acetate/hexanes that had been cooled to 0 °C for several days. The detailed description for the crystallographic data collection and refinement details are given in the SI (Table S2). The determined structure of **HDDB_{in-out}** and **HDDB_{in-in}** are shown in Figure S5. ^1H NMR (dichloromethane- d_2 , 400 MHz): δ = 0.74 (1H, s), 1.24 (6H, s), 2.58 (6H, s), 5.79–5.83 (2H, d, J = 10.5 Hz), 6.23–6.26 (2H, d, J = 9.06 Hz), 6.55–6.58 (2H, d, J = 7.81 Hz), 6.93–6.96 (2H, d, J = 10.7 Hz), 7.05–7.08 (2H, d, J = 7.91 Hz), 7.29–7.31 (4H, d, J = 5.81 Hz), 7.52–7.57 (2H, dd, J = 2.70, 8.99 Hz), 7.94–7.95 (2H, d, J = 2.69 Hz), 8.58–8.60 (2H, d, J = 5.23 Hz) ppm (Figure S6). ^{13}C NMR (acetone- d_6 , 400 MHz): δ = 21.00, 25.65, 31.66, 52.51, 108.23, 114.92, 118.80, 120.65, 120.89, 121.17, 122.99, 125.13, 125.64, 129.69, 131.38, 132.90, 136.40, 141.08, 145.72, 149.54, 160.00 ppm (Figure S6). FTIR (neat, cm^{-1}): 3327, 2972, 2934, 2364, 2343, 2288, 2191, 2150, 2043, 1984, 1920, 1648, 1613, 1594, 1576, 1519, 1467, 1386, 1340, 1282, 1230, 1180, 1149, 1125, 1090, 1074, 1059, 1020, 951, 928, 906, 833, 803, 747, 706, 682, 661 (Figure S11). HRMS (ESI, m/z) calculated for $\text{C}_{48}\text{H}_{40}\text{N}_6\text{O}_6$ $[\text{M}+\text{H}]^+$ 797.3088, found 797.3094.

Preparation of 1 ($\text{Zn}_2\text{C}_{63}\text{H}_{40}\text{N}_4\text{O}_{11}\text{Br}_2$, $\text{Zn}_2(\text{DBTD})(\text{TNDS})$).

MOF 1 was prepared using a slightly modified literature procedure.¹⁰⁹ In a one-dram vial, $\text{Zn}(\text{NO}_3)_2 \cdot 6\text{H}_2\text{O}$ (18 mg, 59 μmol), H_4DBTD (5.4 mg, 7.5 μmol), and **TNDS** (5.0 mg, 10.5 μmol) were dissolved in 0.8 mL of DMF with 0.1 μL of HCl, followed by sonication. The resulting solution was placed in a preheated oven at 80 °C for 24 h, then cooled down to room temperature over 2 h. Red almond-shaped crystals of **1** (13.1 mg, 9.4 μmol) were isolated in 90% yield. The detailed description for the crystallographic data collection and refinement details are given in the SI (Table S3). The determined structure of **1** is shown in Figure S7. FTIR (neat, cm^{-1}): 3445, 3069, 2931, 2880, 1642, 1609, 1558, 1495, 1460, 1435, 1385, 1338, 1275, 1255, 1220, 1178, 1151, 1092 (Figure S8). The PXRD pattern of **1** is shown in Figure S8. The ^1H NMR spectra and mass-spectrometry data of digested **1** are shown in Figure S9. The experimental procedure utilized for MOF digestion can be found in the SI.

Preparation of 2 ($\text{Zn}_2\text{C}_{82}\text{H}_{56}\text{N}_6\text{O}_{14}\text{Br}_2$, $\text{Zn}_2(\text{DBTD})(\text{HDDDB})$).

MOF 2 was prepared using a slightly modified literature procedure.²⁹ In a one-dram vial, $\text{Zn}(\text{NO}_3)_2 \cdot 6\text{H}_2\text{O}$ (8.8 mg, 30 μmol), H_4DBTD (2.5 mg, 3.5 μmol), and **HDDDB** (4.8 mg, 6.0 μmol) were dissolved in 1 mL of DMF and 0.2 μL of HBF_4 , followed by sonication. The resulting solution was placed in a preheated oven at 85 °C for 18 h, then cooled down to room temperature over 2 h. Deep red oval plate crystals of **2** (9.6 mg, 5.8 μmol) were isolated in 97% yield. The detailed description for the crystallographic data collection and refinement details are given in the SI (Table S3). The determined structure of **2** is shown in Figure S10. FTIR (neat, cm^{-1}): 3450, 2934, 2870, 1660, 1558, 1463, 1436, 1385, 1337, 1316, 1274, 1255, 1221, 1178, 1152, 1090 (Figure S11). PXRD pattern and $^{13}\text{C}\{^1\text{H}\}$ CP-MAS NMR spectrum of **2** are shown in Figures S11 and S12, respectively.

Preparation of 3 ($\text{Zn}_2\text{C}_{59}\text{H}_{44}\text{N}_2\text{O}_8\text{Br}_2$, $\text{Zn}_2(\text{DBTD})(\text{BPMTCC})$).

MOF **3** was prepared using a slightly modified literature procedure.²⁹ In a one-dram vial, Zn(NO₃)₂·6H₂O (35.0 mg, 120 μmol), H₄DBTD (10.0 mg, 13.9 μmol) and BPMTc (9.0 mg, 22 μmol) were dissolved in a solution of 2 mL DMF and one drop of HBF₄, followed by sonication. The resulting solution was placed in a preheated oven at 85 °C for 18 h, then cooled down to room temperature over 2 h. Colorless plate crystals of **3** (13 mg, 10 μmol) were isolated in 75% yield. FTIR (neat, cm⁻¹): 3485, 3067, 2925, 2870, 1665, 1639, 1610, 1556, 1502, 1435, 1385, 1255, 1222, 1177, 1150, 1091. The PXRD pattern of **3** is shown in Figure S13. The ¹H NMR spectra and mass-spectrometry data of digested **3** are shown in Figure S14.

Preparation of 3' (Zn₂C₅₃H₃₀N₂O₄S₂, Zn₂(BPDC)₂(BPMTc)). In a 20 mL vial, Zn(NO₃)₂·6H₂O (7.0 mg, 24 μmol), H₂BPDC (6.0 mg, 25 μmol), and BPMTc (10 mg, 24 μmol) were dissolved in a solution of 2 mL DMF, followed by sonication. The resulting solution was heated at 110 °C in an isothermal oven. After 24 h, the reaction mixture was cooled down to room temperature over 2 h. Light brown rectangular block crystals of **3'** (9.2 mg, 8.9 μmol) were isolated in 74% yield. The detailed description for the crystallographic data collection and refinement details are given in the SI (Table S3). The determined structure of **3'** is shown in Figure S15. FTIR (neat, cm⁻¹): 3410, 3080, 2932, 2866, 1660, 1604, 1545, 1500, 1384, 1253, 1176, 1140, 1095, 1080, 1022, 1005, 859, 840, 800, 770, 704, 681, 660 (Figure S16). The PXRD pattern of **3'** is shown in Figure S16.

Preparation of 4 (Zr₆C₈₁H₇₈O₃₄S₂, Zr₆(Me₂BPDC)₄(BCMTC)_{0.5}). MOF **4** was prepared using a modified synthetic route.⁹⁶ Crystals of Zr₆(Me₂BPDC)₄ (30 mg, 16 μmol) were added to solution of H₂BCMTC (42 mg, 0.12 mmol) in 4 mL of DMF in a one-dram vial. The vial was placed in a preheated oven at 75 °C for 24 h, then cooled to room temperature over two hours. Light tan crystals of **4** (35 mg, 14 μmol) were isolated in 64% yield. FTIR (neat, cm⁻¹): 3450, 2935, 2855, 1657, 1586, 1544, 1495, 1411, 1384, 1255, 1208, 1139, 1091. The PXRD pattern of **4** is shown in Figure S18. The ¹H NMR spectra of digested **4** is shown in Figure S19.

UV-vis, diffuse reflectance, and fluorescence spectroscopies. Steady-state emission spectra were acquired on an Edinburgh FS5 fluorescence spectrometer equipped with a 150 W Continuous Wave Xenon Lamp source for excitation. Emission measurements on solid samples were collected on the powders of the appropriate materials placed inside a 0.5 mm quartz sample holder using the front-facing module. The Ocean Optics JAZ spectrometer was also used for absorbance and diffuse reflectance measurements. An Ocean Optics ISP-REF integrating sphere was connected to the spectrometer using a 450 μm SMA fiber optic cable. A 400 nm long pass filter was placed between an 8.0 mm quartz sample cell with cover and the integrating sphere to filter any UV light from the internal tungsten-halogen lamp. An Ocean Optics WS-1 Spectralon® reflectance standard was placed on the sample cell throughout the measurements. A mounted high-powered LED (M365L2, Thorlabs), λ = 365 nm, was used for *in situ* irradiation of the samples. Before time-resolved UV-vis and diffuse reflectance measurements, the sample background was subtracted to obtain the spectra corresponding to photophysical behavior of the photochromic derivatives.

¹³C CP-MAS NMR Spectroscopy. Solid-state NMR spectra (¹³C CP-MAS) were collected on a Bruker Avance III-HD 500 MHz spectrometer fitted with a 1.9 mm MAS probe. ¹³C{¹H} CP-MAS NMR spectra (125.79 MHz) were collected at ambient temperature with a sample rotation rate of 20 kHz. For cross polarization, 2.0 ms contact time with linear ramping on the ¹H channel and

62.5 kHz field on the ¹³C channel were used. ¹H dipolar decoupling was performed with SPINAL64 modulation and 147 kHz field strength. Free induction decays (2048–5000 transients) were collected with a 27 ms acquisition time over a 400 ppm spectra width with a relaxation delay of 2.0 s.

Other Physical Measurements. FTIR spectra were obtained on a Perkin-Elmer Spectrum 100. NMR spectra were collected on Bruker Avance III-HD 300 and Bruker Avance III 400 MHz NMR spectrometers. ¹³C and ¹H NMR spectra were referenced to natural abundance ¹³C peaks and residual ¹H peaks of deuterated solvents, respectively. Powder X-ray diffraction patterns were recorded on a Rigaku Miniflex II diffractometer with accelerating voltage and current of 30 kV and 15 mA, respectively. The Waters QTOF-I quadrupole time-of-flight and Thermo Scientific Orbitrap Velos Pro mass-spectrometers were used to record the mass-spectra of the prepared compounds.

ASSOCIATED CONTENT

SUPPORTING INFORMATION

The supporting information is available free of charge on the ACS publications website at DOI: X-ray structure refinement data of prepared MOFs, PXRD patterns, FTIR, ¹H, ¹³C, and ¹³C{H} CP MAS NMR spectra. Crystallographic information for C₁₉H₁₆Br₂N₂O₃, **VI**, CCDC 1829891 (CIF); Crystallographic information for TNDS, CCDC 1829888 (CIF); Crystallographic information for C₃₈H₃₂Br₂N₄O₆, **VII'**, CCDC 1829895 (CIF); Crystallographic information for Hddb_{in-in}, CCDC 1829894 (CIF); Crystallographic information for Hddb_{in-out}, CCDC 1829893 (CIF); Crystallographic information for **1**, (Zn₂(DBTD)(TNDS)), CCDC 1829890 (CIF); Crystallographic information for **2**, (Zn₂(DBTD)(Hddb)), CCDC 1829889 (CIF); Crystallographic information for **3'**, (Zn₂(BPDC)₂(BPMTc)), CCDC 1829892 (CIF).

AUTHOR INFORMATION

Corresponding Author

*shustova@sc.edu

ORCID

Natalia B. Shustova: 000-0003-3952-1949

Author Contributions

The manuscript was written through contributions of all authors. / All authors have given approval to the final version of the manuscript. / ‡These authors contributed equally.

Notes

This author declares no competing financial interests.

ACKNOWLEDGMENT

N.B.S. gratefully acknowledges support from the NSF CAREER Award (DMR-1553634), the Sloan Research Fellowship provided by the Alfred P. Sloan foundation, and a Cottrell Scholar Award from the Research Corporation for Science Advancement.

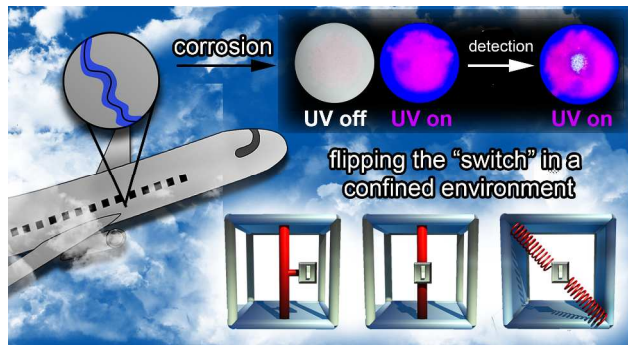
REFERENCES

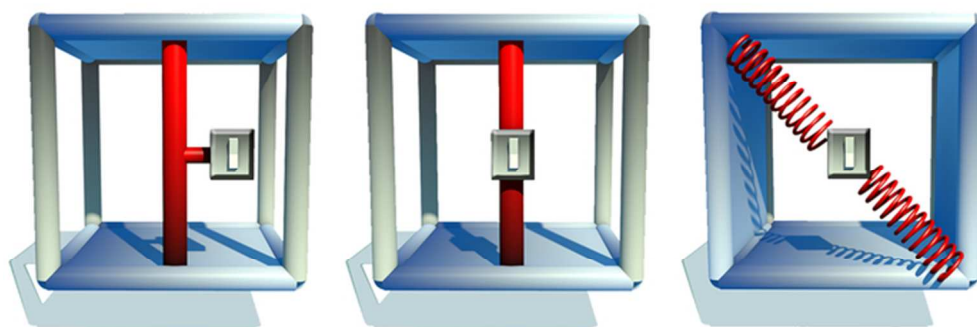
- 1) Brown, J. W.; Henderson, B. L.; Kiesz, M. D.; Whalley, A. C.; Morris, W.; Grunder, S.; Deng, H.; Furukawa, H.; Zink, J. I.; Stoddart, J. F.; Yaghi, O. M. *Chem. Sci.* **2013**, *4*, 2858–2864.
- 2) Yanai, N.; Uemura, T.; Inoue, M.; Matsuda, R.; Fukushima, T.; Tsujimoto, M.; Isoda, S.; Kitagawa, S. *J. Am. Chem. Soc.* **2012**,

- 134, 4501–4504.
- 1 (3) Tian, Z.; Wu, W.; Wan, W.; Li, A. D. Q. *J. Am. Chem. Soc.* **2011**, *133*, 16092–16100.
 - 2 (4) Simeth, N. A.; Crespi, S.; Fagnoni, M.; König, B. *J. Am. Chem. Soc.* **2018**, *140*, 2940–2946.
 - 3 (5) Kashiwara, R.; Morimoto, M.; Ito, S.; Miyasaka, H.; Irie, M. *J. Am. Chem. Soc.* **2017**, *139*, 16498–16501.
 - 4 (6) Liu, Z.; Wang, H. I.; Narita, A.; Chen, Q.; Mics, Z.; Turchinovich, D.; Kläui, M.; Bonn, M.; Müllen, K. *J. Am. Chem. Soc.* **2017**, *139*, 9443–9446.
 - 5 (7) Potisek, S. L.; Davis, D. A.; Sottos, N. R.; White, S. R.; Moore, J. S. *J. Am. Chem. Soc.* **2007**, *129*, 13808–13809.
 - 6 (8) Xing, Q. J.; Li, N. J.; Chen, D. Y.; Sha, W. W.; Jiao, Y.; Qi, X. X.; Xu, Q. F.; Lu, J. M. *J. Mater. Chem. B* **2014**, *2*, 1182–1189.
 - 7 (9) Cotí, K. K.; Belowich, M. E.; Liong, M.; Ambrogio, M. W.; Lau, Y. A.; Khatib, H. A.; Zink, J. I.; Khashab, N. M.; Stoddart, J. F. *Nanoscale* **2009**, *1*, 16–39.
 - 8 (10) Bajpai, A. K.; Shukla, S. K.; Bhanu, S.; Kankane, S. *Prog. Polym. Sci.* **2008**, *33*, 1088–1118.
 - 9 (11) Wilkinson, M.; Kafizas, A.; Bawaked, S. M.; Obaid, A. Y.; Al-Thabaiti, S. A.; Basahel, S. N.; Carmalt, C. J.; Parkin, I. P. *ACS Comb. Sci.* **2013**, *15*, 309–319.
 - 10 (12) Liou, J.-C.; Teng, M.-C.; Tsai, Y.-S.; Lin, E.-C.; Chen, B.-Y. *Mol. Vis.* **2015**, *21*, 846–856.
 - 11 (13) Sumi, T.; Takagi, Y.; Yagi, A.; Morimoto, M.; Irie, M. *Chem. Commun.* **2014**, *50*, 3928–3930.
 - 12 (14) Szacilowski, K. *Chem. Rev.* **2008**, *108*, 3481–3548.
 - 13 (15) Wagner, K.; Byrne, R.; Zanon, M.; Gambhir, S.; Dennany, L.; Breukers, R.; Higgins, M.; Wagner, P.; Diamond, D.; Wallace, G. G.; Officer, D. L. *J. Am. Chem. Soc.* **2011**, *133*, 5453–5462.
 - 14 (16) Kumar, S.; Van Herpt, J. T.; Gengler, R. Y. N.; Feringa, B. L.; Rudolf, P.; Chiechi, R. C. *J. Am. Chem. Soc.* **2016**, *138*, 12519–12526.
 - 15 (17) Zhu, L.; Zhu, M. Q.; Hurst, J. K.; Li, A. D. Q. *J. Am. Chem. Soc.* **2005**, *127*, 8968–8970.
 - 16 (18) Williams, D. E.; Rietman, J. A.; Jaier, J. M.; Tan, R.; Greytak, A. B.; Smith, M. D.; Krause, J. A.; Shustova, N. B. *J. Am. Chem. Soc.* **2014**, *136*, 11886–11889.
 - 17 (19) Patel, D. G.; Walton, I. M.; Cox, J. M.; Gleason, C. J.; Butzer, D. R.; Benedict, J. B. *Chem. Commun.* **2014**, *50*, 2653.
 - 18 (20) Schulz-Senft, M.; Gates, P. J.; Sönnichsen, F. D.; Staubitz, A. *Dye. Pigment.* **2017**, *136*, 292–301.
 - 19 (21) Irie, M. *Photochem. Photobiol. Sci.* **2010**, *9*, 1535.
 - 20 (22) Yaghi, O. M.; O’Keeffe, M.; Ockwig, N. W.; Chae, H. K.; Eddaoudi, M.; Kim, J. *Nature* **2003**, *423*, 705–714.
 - 21 (23) Flaig, R. W.; Osborn Popp, T. M.; Fracaroli, A. M.; Kapustin, E. A.; Kalmutski, M. J.; Altamimi, R. M.; Fathieh, F.; Reimer, J. A.; Yaghi, O. M. *J. Am. Chem. Soc.* **2017**, *139*, 12125–12128.
 - 22 (24) Helal, A.; Yamani, Z. H.; Cordova, K. E.; Yaghi, O. M. *Nat. Sci. Rev.* **2017**, *4*, 296–298.
 - 23 (25) Parent, L. R.; Pham, C. H.; Patterson, J. P.; Denny, M. S.; Cohen, S. M.; Gianneschi, N. C.; Paesani, F. *J. Am. Chem. Soc.* **2017**, *139*, 13973–13976.
 - 24 (26) Rieth, A. J.; Dincă, M. *J. Am. Chem. Soc.* **2018**, *140*, 3461–3466.
 - 25 (27) Ji, P.; Feng, X.; Veroneau, S. S.; Song, Y.; Lin, W. *J. Am. Chem. Soc.* **2017**, *139*, 15600–15603.
 - 26 (28) Vogelsberg, C. S.; Uribe-Romo, F. J.; Lipton, A. S.; Yang, S.; Houk, K. N.; Brown, S.; Garcia-Garibay, M. A. *Proc. Natl. Acad. Sci.* **2017**, *114*, 13613–13618.
 - 27 (29) Park, J.; Feng, D.; Yuan, S.; Zhou, H. C. *Angew. Chem. Int. Ed.* **2015**, *54*, 430–435.
 - 28 (30) Liu, C.; Luo, T.-Y.; Feura, E. S.; Zhang, C.; Rosi, N. L. *J. Am. Chem. Soc.* **2015**, *137*, 10508–10511.
 - 29 (31) Usov, P. M.; Huffman, B.; Epley, C. C.; Kessinger, M. C.; Zhu, J.; Maza, W. A.; Morris, A. J. *ACS Appl. Mater. Interfaces* **2017**, *9*, 33539–33543.
 - 30 (32) Alsbaiee, A.; Smith, B. J.; Xiao, L.; Ling, Y.; Helbling, D. E.; Dichtel, W. R. *Nature* **2016**, *529*, 190–194.
 - 31 (33) Whittemore, T. J.; White, T. A.; Turro, C. *J. Am. Chem. Soc.* **2018**, *140*, 229–234.
 - 32 (34) Feng, L.; Yuan, S.; Zhang, L.-L.; Tan, K.; Li, J.-L.; Kirchon, A.; Liu, L.-M.; Zhang, P.; Han, Y.; Chabal, Y. J.; Zhou, H.-C. *J. Am. Chem. Soc.* **2018**, *140*, 2363–2372.
 - 33 (35) Zhu, J.; Usov, P. M.; Xu, W.; Celis-Salazar, P. J.; Lin, S.; Kessinger, M. C.; Landaverde-Alvarado, C.; Cai, M.; May, A. M.; Slobodnick, C.; Zhu, D.; Senanayake, S. D.; Morris, A. J. *J. Am. Chem. Soc.* **2018**, *140*, 993–1003.
 - 34 (36) Smith, M. K.; Jensen, K. E.; Pivak, P. A.; Mirica, K. A. *Chem. Mater.* **2016**, *28*, 5264–5268.
 - 35 (37) Kim, H.; Yang, S.; Rao, S. R.; Narayanan, S.; Kapustin, E. A.; Furukawa, H.; Umans, A. S.; Yaghi, O. M.; Wang, E. N. *Science* **2017**, *356*, 430–434.
 - 36 (38) Zhao, Y.; Lee, S. Y.; Becknell, N.; Yaghi, O. M.; Angell, C. A. *J. Am. Chem. Soc.* **2016**, *138*, 10818–10821.
 - 37 (39) Li, B.; Cui, X.; O’Nolan, D.; Wen, H.-M.; Jiang, M.; Krishna, R.; Wu, H.; Lin, R.-B.; Chen, Y.-S.; Yuan, D.; Xing, H.; Zhou, W.; Ren, Q.; Qian, G.; Zaworotko, M.; Chen, B. *Adv. Mater.* **2017**, *29*, 1704210.
 - 38 (40) Lin, Z.; Thacker, N. C.; Sawano, T.; Drake, T.; Ji, P.; Lan, G.; Cao, L.; Liu, S.; Wang, C.; Lin, W. *Chem. Sci.* **2018**, *9*, 143–151.
 - 39 (41) Yuan, S.; Feng, L.; Wang, K.; Pang, J.; Bosch, M.; Lollar, C.; Sun, Y.; Qin, J.; Yang, X.; Zhang, P.; Wang, Q.; Zou, L.; Zhang, Y.; Zhang, L.; Fang, Y.; Li, J.; Zhou, H. C. *Adv. Mater.* **2018**, *30*, 1704303.
 - 40 (42) Spore, A. B.; Rosi, N. L. *CrystEngComm* **2017**, *19*, 5417–5421.
 - 41 (43) Milner, P. J.; Martell, J. D.; Siegelman, R. L.; Gygi, D.; Weston, S. C.; Long, J. R. *Chem. Sci.* **2018**, *9*, 160–174.
 - 42 (44) Plonka, A. M.; Banerjee, D.; Woerner, W. R.; Zhang, Z.; Nijem, N.; Chabal, Y. J.; Li, J.; Parise, J. B. *Angew. Chem. Int. Ed.* **2013**, *52*, 1692–1695.
 - 43 (45) Walton, I. M.; Cox, J. M.; Coppin, J. A.; Linderman, C. M.; Patel, D. G.; Benedict, J. B. *Chem. Commun.* **2013**, *49*, 8012–8014.
 - 44 (46) Park, J.; Yuan, D.; Pham, K. T.; Li, J. R.; Yakovenko, A.; Zhou, H. C. *J. Am. Chem. Soc.* **2012**, *134*, 99–102.
 - 45 (47) Walton, I. M.; Cox, J. M.; Mitchell, T. B.; Bizier, N. P.; Benedict, J. B. *CrystEngComm* **2016**, *18*, 7972–7977.
 - 46 (48) Gong, L. Le; Yao, W. T.; Liu, Z. Q.; Zheng, A. M.; Li, J. Q.; Feng, X. F.; Ma, L. F.; Yan, C. S.; Luo, M. B.; Luo, F. *J. Mater. Chem. A* **2017**, *5*, 7961–7967.
 - 47 (49) Lyndon, R.; Konstas, K.; Ladewig, B. P.; Southon, P. D.; Kepert, P. C. J.; Hill, M. R. *Angew. Chem. Int. Ed.* **2013**, *52*, 3695–3698.
 - 48 (50) Fu, W.-Q.; Liu, M.; Gu, Z.-G.; Chen, S.-M.; Zhang, J. *Cryst. Growth Des.* **2016**, *16*, 5487–5492.
 - 49 (51) Healey, K.; Liang, W.; Southon, P. D.; Church, T. L.; D’Alessandro, D. M. *J. Mater. Chem. A* **2016**, *4*, 10816–10819.
 - 50 (52) Zhang, F.; Zou, X.; Feng, W.; Zhao, X.; Jing, X.; Sun, F.; Ren, H.; Zhu, G. *J. Mater. Chem.* **2012**, *48*, 25019–25026.
 - 51 (53) Schwartz, H. A.; Olthof, S.; Schaniel, D.; Meerholz, K.; Ruschewitz, U. *Inorg. Chem.* **2017**, *56*, 13100–13110.
 - 52 (54) Yaghi, O. M. *J. Am. Chem. Soc.* **2016**, *138*, 15507–15509.
 - 53 (55) Schoedel, A.; Li, M.; Li, D.; O’Keeffe, M.; Yaghi, O. M. *Chem. Rev.* **2016**, *116*, 12466–12535.
 - 54 (56) Schukraft, G. E. M.; Ayala, S.; Dick, B. L.; Cohen, S. M. *Chem. Commun.* **2017**, *53*, 10684–10687.
 - 55 (57) Gong, X.; Young, R. M.; Hartlieb, K. J.; Miller, C.; Wu, Y.; Xiao, H.; Li, P.; Hafezi, N.; Zhou, J.; Ma, L.; Cheng, T.; Goddard, W.; Farha, O. K. Hupp, J. T.; Wasielewski, M. R.; Stoddart, J. F. *J. Am. Chem. Soc.* **2017**, *139*, 4107–4116.
 - 56 (58) Rieth, A. J.; Yang, S.; Wang, E. N.; Dincă, M. *ACS Cent. Sci.* **2017**, *3*, 668–672.
 - 57 (59) Campbell, M.; Dincă, M. *Sensors* **2017**, *17*, 1108.
 - 58 (60) Gonzalez, M. I.; Kapelewski, M. T.; Bloch, E. D.; Milner, P. J.; Reed, D. A.; Hudson, M. R.; Mason, J. A.; Barin, G.; Brown, C. M.; Long, J. R. *J. Am. Chem. Soc.* **2018**, *140*, 3412–3422.
 - 59 (61) Milner, P. J.; Siegelman, R. L.; Forse, A. C.; Gonzalez, M. I.; Runčevski, T.; Martell, J. D.; Reimer, J. A.; Long, J. R. *J. Am. Chem. Soc.* **2017**, *139*, 13541–13553.
 - 60 (62) Hu, Z.; Deibert, B. J.; Li, J. *Chem. Soc. Rev.* **2014**, *43*, 5815–5840.
 - 61 (63) Epley, C. C.; Roth, K. L.; Lin, S.; Ahrenholtz, S. R.; Grove, T. Z.; Morris, A. J. *Dalt. Trans.* **2017**, *46*, 4917–4922.
 - 62 (64) Chen, X.; Bu, X.; Lin, Q.; Mao, C.; Zhai, Q.-G.; Wang, Y.; Feng, P. *Chem. - A Eur. J.* **2017**, *23*, 11913–11919.
 - 63 (65) Jagadesan, P.; Whittemore, T.; Beirl, T.; Turro, C.; McGrier, P. L. *Chem. - A Eur. J.* **2017**, *23*, 917–925.
 - 64 (66) Ling, Y.; Klemes, M. J.; Xiao, L.; Alsbaiee, A.; Dichtel, W. R.;

- 1 Helbling, D. E. *Environ. Sci. Technol.* **2017**, *51*, 7590–7598.
- 2 (67) Jiang, J.; Furukawa, H.; Zhang, Y. B.; Yaghi, O. M. *J. Am. Chem. Soc.* **2016**, *138*, 10244–10251.
- 3 (68) Fracaroli, A. M.; Siman, P.; Nagib, D. A.; Suzuki, M.; Furukawa, H.; Toste, F. D.; Yaghi, O. M. *J. Am. Chem. Soc.* **2016**, *138*, 8352–8355.
- 4 (69) Ko, M.; Aykanat, A.; Smith, M.; Mirica, K. *Sensors* **2017**, *17*, 2192.
- 5 (70) Yu, X.; Wang, L.; Cohen, S. M. *CrystEngComm* **2017**, *19*, 4126–4136.
- 6 (71) Haikal, R. R.; Hua, C.; Perry, J. J.; O’Nolan, D.; Syed, I.; Kumar, A.; Chester, A. H.; Zaworotko, M. J.; Yacoub, M. H.; Alkordi, M. H. *ACS Appl. Mater. Interfaces* **2017**, *9*, 43520–43528.
- 7 (72) Bobbitt, N. S.; Mendonca, M. L.; Howarth, A. J.; Islamoglu, T.; Hupp, J. T.; Farha, O. K.; Snurr, R. Q. *Chem. Soc. Rev.* **2017**, *46*, 3357–3385.
- 8 (73) Ji, P.; Solomon, J. B.; Lin, Z.; Johnson, A.; Jordan, R. F.; Lin, W. *J. Am. Chem. Soc.* **2017**, *139*, 11325–11328.
- 9 (74) Huang, N.; Yuan, S.; Drake, H.; Yang, X.; Pang, J.; Qin, J.; Li, J.; Zhang, Y.; Wang, Q.; Jiang, D.; Zhou, H.-C. *J. Am. Chem. Soc.* **2017**, *139*, 18590–18597.
- 10 (75) Luo, T.-Y.; Liu, C.; Eliseeva, S. V.; Muldoon, P. F.; Petoud, S.; Rosi, N. L. *J. Am. Chem. Soc.* **2017**, *139*, 9333–9340.
- 11 (76) Semino, R.; Moreton, J. C.; Ramsahye, N. A.; Cohen, S. M.; Maurin, G. *Chem. Sci.* **2018**, *9*, 315–324.
- 12 (77) Yuan, S.; Lu, W.; Chen, Y.-P.; Zhang, Q.; Liu, T.-F.; Feng, D.; Wang, X.; Qin, J.; Zhou, H.-C. *J. Am. Chem. Soc.* **2015**, *137*, 3177–3180.
- 13 (78) Kobatake, S.; Shibata, K.; Uchida, K.; Irie, M. *J. Am. Chem. Soc.* **2000**, *122*, 12135–12141.
- 14 (79) Irie, M.; Lifka, T.; Kobatake, S.; Kato, N. *J. Am. Chem. Soc.* **2000**, *122*, 4871–4876.
- 15 (80) Irie, M.; Fukaminato, T.; Matsuda, K.; Kobatake, S. *Chem. Rev.* **2014**, *114*, 12174–12277.
- 16 (81) Kitagawa, D.; Tsujioka, H.; Tong, F.; Dong, X.; Bardeen, C. J.; Kobatake, S. *J. Am. Chem. Soc.* **2018**, *140*, 4208–4212.
- 17 (82) Tam, E. S.; Parks, J. J.; Shum, W. W.; Zhong, Y. W.; Santiago-Berrios, M. B.; Zheng, X.; Yang, W.; Chan, G. K. L.; Abreuña, H. D.; Ralph, D. C. *ACS Nano* **2011**, *5*, 5115–5123.
- 18 (83) Lucas, L. N.; Jong, J. J.; Esch, J. H.; Kellogg, R. M.; Feringa, B. L. *Eur. J. Org. Chem.* **2003**, *2003*, 155–166.
- 19 (84) Kobatake, S.; Uchida, K.; Tsuchida, E.; Irie, M. *Chem. Commun.* **2002**, 2804–2805.
- 20 (85) Klajn, R. *Chem. Soc. Rev.* **2014**, *43*, 148–184.
- 21 (86) Krysanov, S. A.; Alfimov, M. V. *Chem. Phys. Lett.* **1982**, *91*, 77–80.
- 22 (87) Swansburg, S.; Buncel, E.; Lemieux, R. P. *J. Am. Chem. Soc.* **2000**, *122*, 6594–6600.
- 23 (88) Kobatake, S.; Takami, S.; Muto, H.; Ishikawa, T.; Irie, M. *Nature* **2007**, *446*, 778–781.
- 24 (89) Wojtyk, J. T. C.; Wasey, A.; Kazmaier, P. M.; Hoz, S.; Buncel, E. *J. Phys. Chem. A* **2000**, *104*, 9046–9055.
- 25 (90) Udayabhaskararao, T.; Kundu, P. K.; Ahrens, J.; Klajn, R. *ChemPhysChem* **2016**, *76100*, 1805–1809.
- 26 (91) Kundu, P. K.; Olsen, G. L.; Kiss, V.; Klajn, R. *Nat. Commun.* **2014**, *5*, 1–9.
- 27 (92) Maya, F.; Tour, J. M. *Tetrahedron* **2004**, *60*, 81–92.
- 28 (93) Benniston, A. C.; Harriman, A.; Howell, S. L.; Li, P.; Lydon, D. P. *J. Org. Chem.* **2007**, *72*, 888–897.
- 29 (94) Kundu, P. K.; Lerner, A.; Kučanda, K.; Leitus, G.; Klajn, R. *J. Am. Chem. Soc.* **2014**, *136*, 11276–11279.
- 30 (95) Starzak, M. E. *Mathematical Methods in Chemistry and Physics*; Springer US: Boston, MA, 1989.
- 31 (96) Dolgoplova, E. A.; Ejegbavwo, O. A.; Martin, C. R.; Smith, M. D.; Setyawan, W.; Karakalos, S. G.; Henager, C. H.; Zur Loye, H. C.; Shustova, N. B. *J. Am. Chem. Soc.* **2017**, *139*, 16852–16861.
- 32 (97) Yuan, S.; Chen, Y. P.; Qin, J. S.; Lu, W.; Zou, L.; Zhang, Q.; Wang, X.; Sun, X.; Zhou, H. C. *J. Am. Chem. Soc.* **2016**, *138*, 8912–8919.
- 33 (98) Harada, J.; Kawazoe, Y.; Ogawa, K. *Chem. Commun.* **2010**, *46*, 2593–2595.
- 34 (99) Gentili, P. L.; Nocchetti, M.; Miliani, C.; Favaro, G. *New J. Chem.* **2004**, *28*, 379–386.
- 35 (100) Bénard, S.; Yu, P. *Adv. Mater.* **2000**, *12*, 48–50.
- 36 (101) Whelan, J.; Abdallah, D.; Wojtyk, J.; Buncel, E.; Hurst, J. K.; Li, A. D. Q.; Lemieux, R. P.; Buncel, E.; Samat, A.; Guglielmetti, R.; Roma, S.; Salluce, N. *J. Mater. Chem.* **2010**, *20*, 5727–5735.
- 37 (102) Florea, L.; McKeon, A.; Diamond, D.; Benito-Lopez, F. *Langmuir* **2013**, *29*, 2790–2797.
- 38 (103) Breslin, V. M.; Garcia-Garibay, M. A. *Cryst. Growth Des.* **2017**, *17*, 637–642.
- 39 (104) Shoji, H.; Kitagawa, D.; Kobatake, S. *New J. Chem.* **2014**, *38*, 933–941.
- 40 (105) Miyasaka, H.; Nobuto, T.; Itaya, A.; Tamai, N.; Irie, M. *Chem. Phys. Lett.* **1997**, *269*, 281–285.
- 41 (106) Irie, M.; Lifka, T.; Uchida, K.; Kobatake, S.; Shindo, Y. *Chem. Commun.* **1999**, 747–750.
- 42 (107) Tani, K.; Ishibashi, Y.; Miyasaka, H.; Kobatake, S.; Irie, M. *J. Phys. Chem. C* **2008**, *112*, 11150–11157.
- 43 (108) Irie, M.; Sayo, K. *J. Phys. Chem.* **1992**, *96*, 7671–7674.
- 44 (109) Farha, O. K.; Malliakas, C. D.; Kanatzidis, M. G.; Hupp, J. T. *J. Am. Chem. Soc.* **2010**, *132*, 950–952.
- 45 (110) Burrows, A. D.; Frost, C. G.; Mahon, M. F.; Richardson, C. *Chem. Commun.* **2009**, 4218–4220.

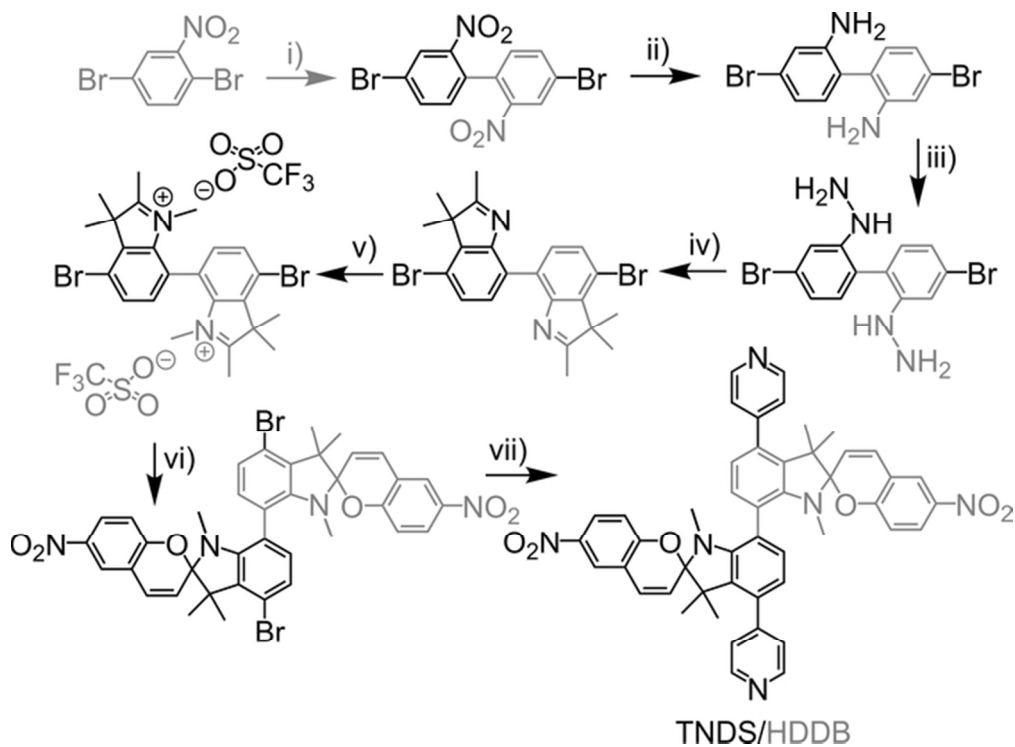
1
2
3
4
5
6
7
8
9
10
11
12
13
14
15
16
17
18
19
20
21
22
23
24
25
26
27
28
29
30
31
32
33
34
35
36
37
38
39
40
41
42
43
44
45
46
47
48
49
50
51
52
53
54
55
56
57
58
59
60





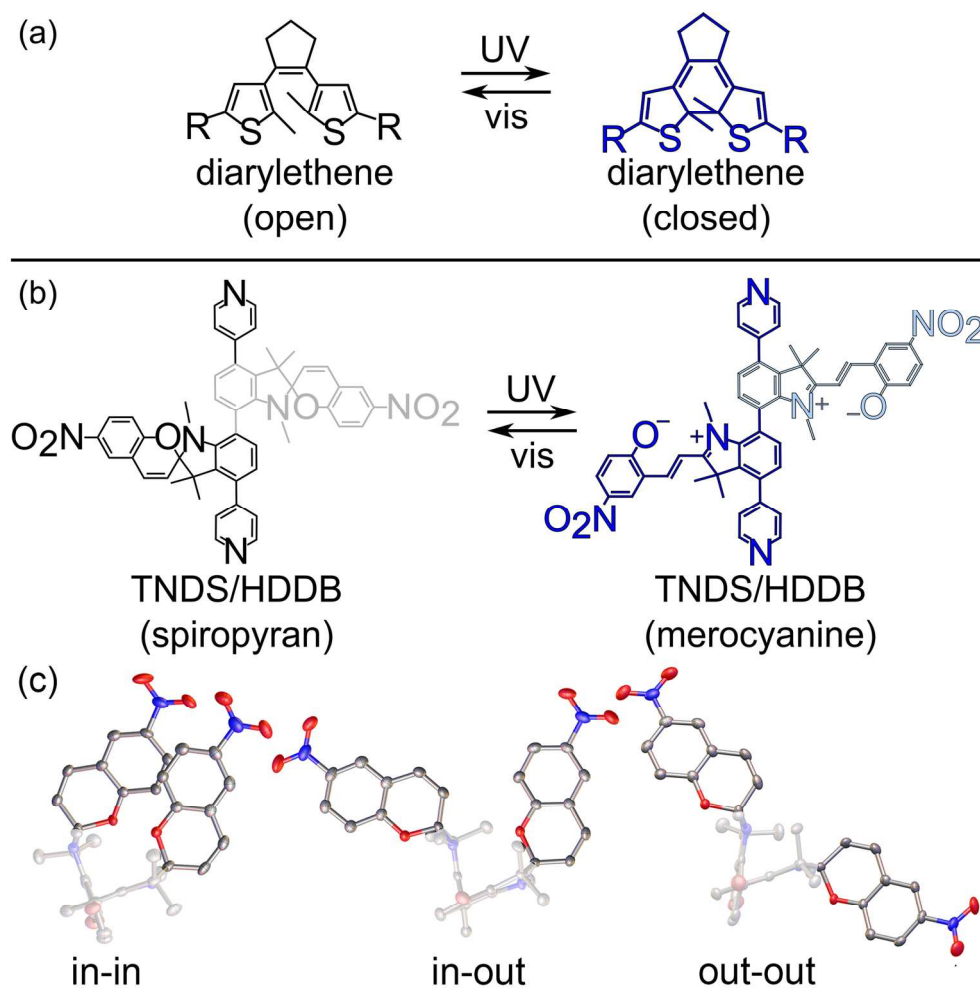
A schematic representation of coordinatively immobilized photochromic derivatives inside the metal-organic rigid scaffold. The photochromic moiety integrated as (left) a side group on the organic linker, (middle) as a framework backbone, and (right) as a capping linker⁸⁶ with the size similar to the framework pocket. A grey "photoswitch" symbol indicates a position of photochromic unit.

29x10mm (600 x 600 DPI)



Scheme 2. Reaction scheme for the synthesis of TNDS (black) and HDDB (grey)^a
 a i) Cu powder, DMF, 120 °C 4 h; ii) SnCl₂, HCl, EtOH, reflux 12 h; iii) NaNO₂, HCl, 0 °C 1 h / CO(NH₂)₂, 0 °C 10 min / SnCl₂, 0 °C, 4 h; iv) 3-methyl-2-butanone, reflux 3 h / H₂SO₄, EtOH, reflux 3 h; v) Et₂O, hexanes, methyl trifluoromethanesulfonate, room temperature, 8 h; vi) 2-hydroxy-5-nitrobenzaldehyde, EtOH, piperidine, reflux 8 h; vii) pyridine-4-boronic acid, PdCl₂(PPh₃)₂, CuCl, Na₂CO₃, DMF, 120 °C, 48 h.

61x44mm (300 x 300 DPI)



39 Figure 1. (a) Photoisomerization of the diarylethene-based and (b) spiropyran derivatives. (c) For simplicity,
40 structural differences of "in-in", "in-out", and "out-out" diastereoisomers are shown on the example of the
41 brominated precursor (Scheme 2) of HDDB. Displacement ellipsoids drawn at the 60% probability level.
42 Gray, blue, and red spheres represent C, N, and O atoms, respectively.

43 83x82mm (600 x 600 DPI)

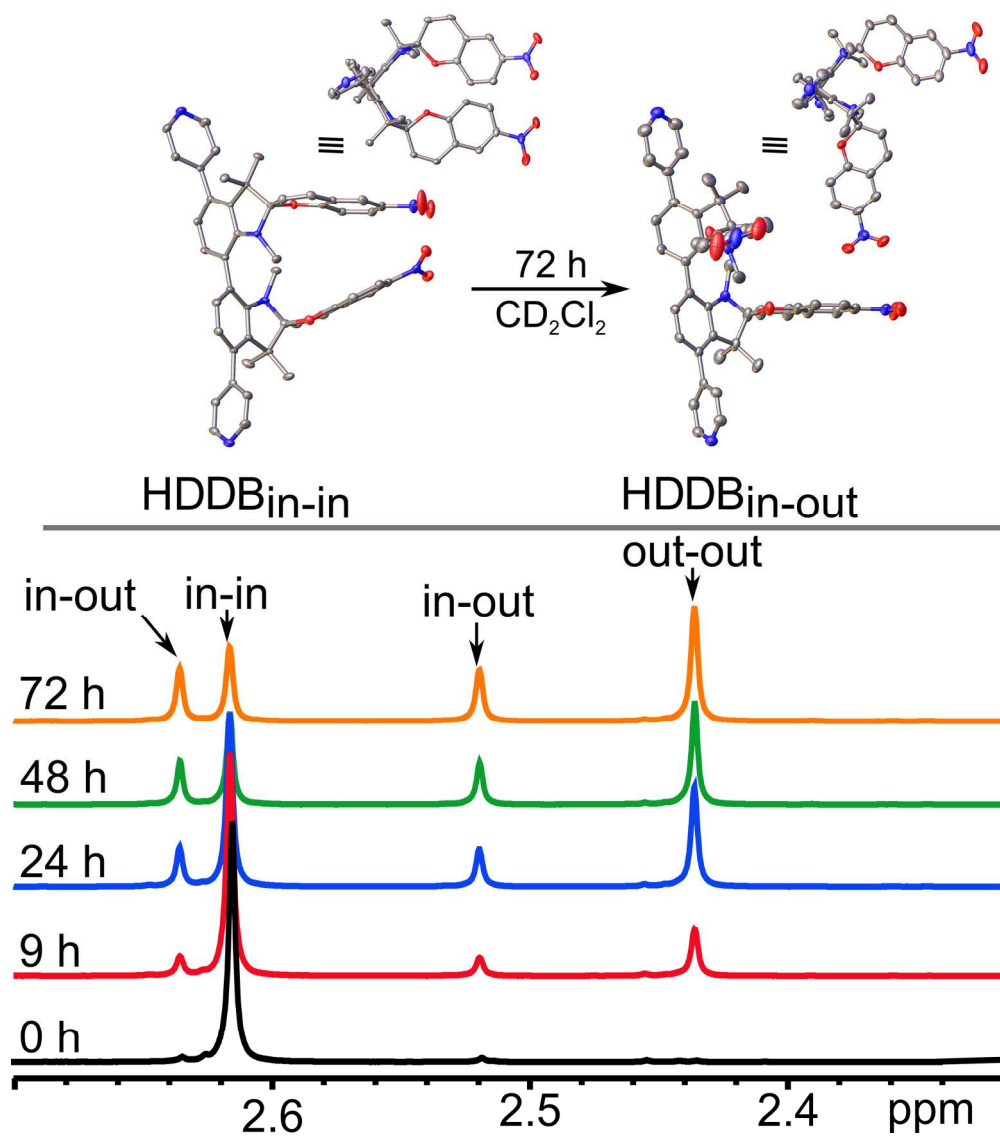
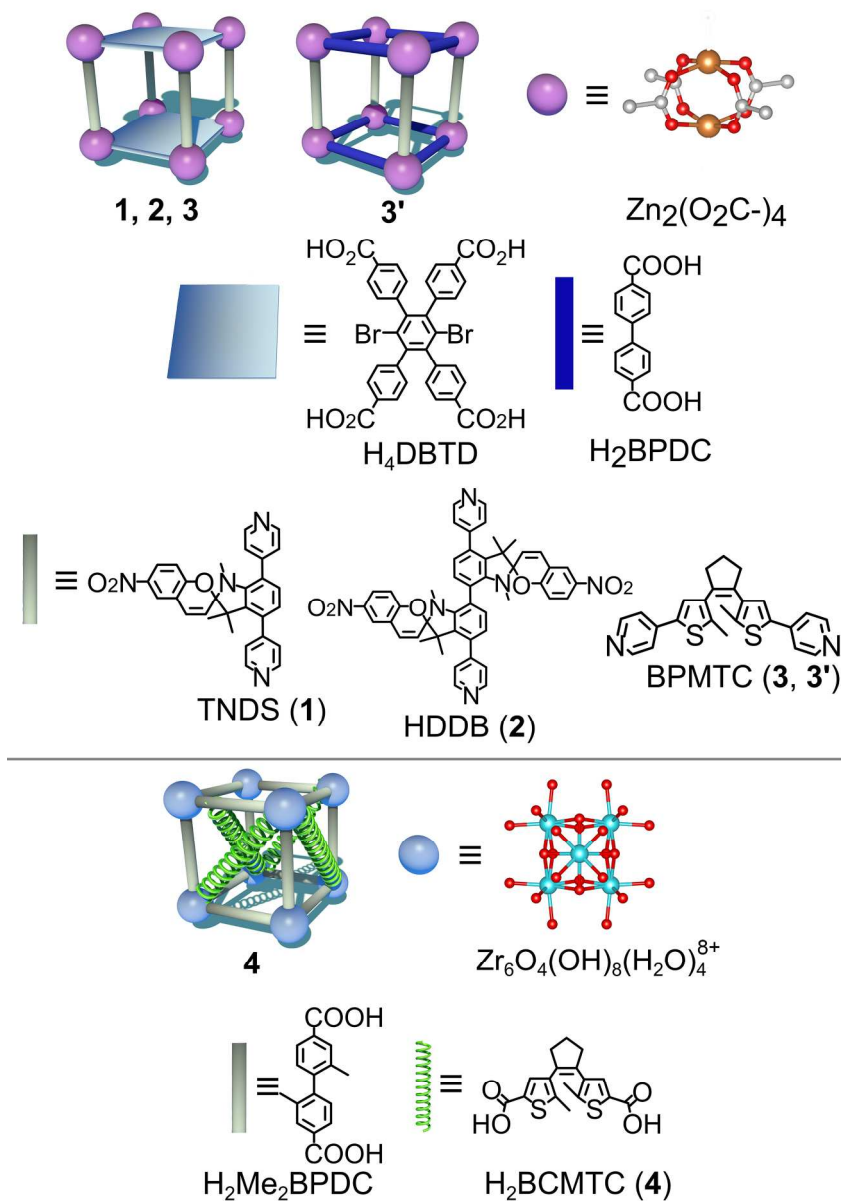


Figure 2. (top) Single crystal X-ray structures of HDDBin-in and HDDBin-out. Two orientations of each diastereoisomer are shown. Displacement ellipsoids drawn at the 60% probability level. Gray, blue, and red spheres represent C, N, and O atoms, respectively. (bottom) For simplicity, a methyl region of the ¹H NMR spectra corresponding to thermal equilibration of HDDBin-in to HDDBin-out and HDDBin-out to HDDBin-out in CD₂Cl₂ is shown at t = 0, 9, 24, 48, and 72 h. The rest of the spectra of the HDDBin-in con-version are shown in Figure S22.

94x107mm (600 x 600 DPI)



45 Figure 3. (top) The TNDS, HDDDB, and BPMTTC linkers were used to synthesize 1, 2, and 3 (3'), respectively,
 46 in the presence of H4DBTD (H2BPDC). (bottom) The linker, H2BCMTC, was in-stalled as a capping linker into
 47 an existing MOF framework, $Zr_6(Me_2BPDC)_4,86$ to make 4. Orange, red, teal, and gray spheres correspond
 48 to zinc, oxygen, zirconium, and carbon atoms, respectively

49 118x167mm (600 x 600 DPI)

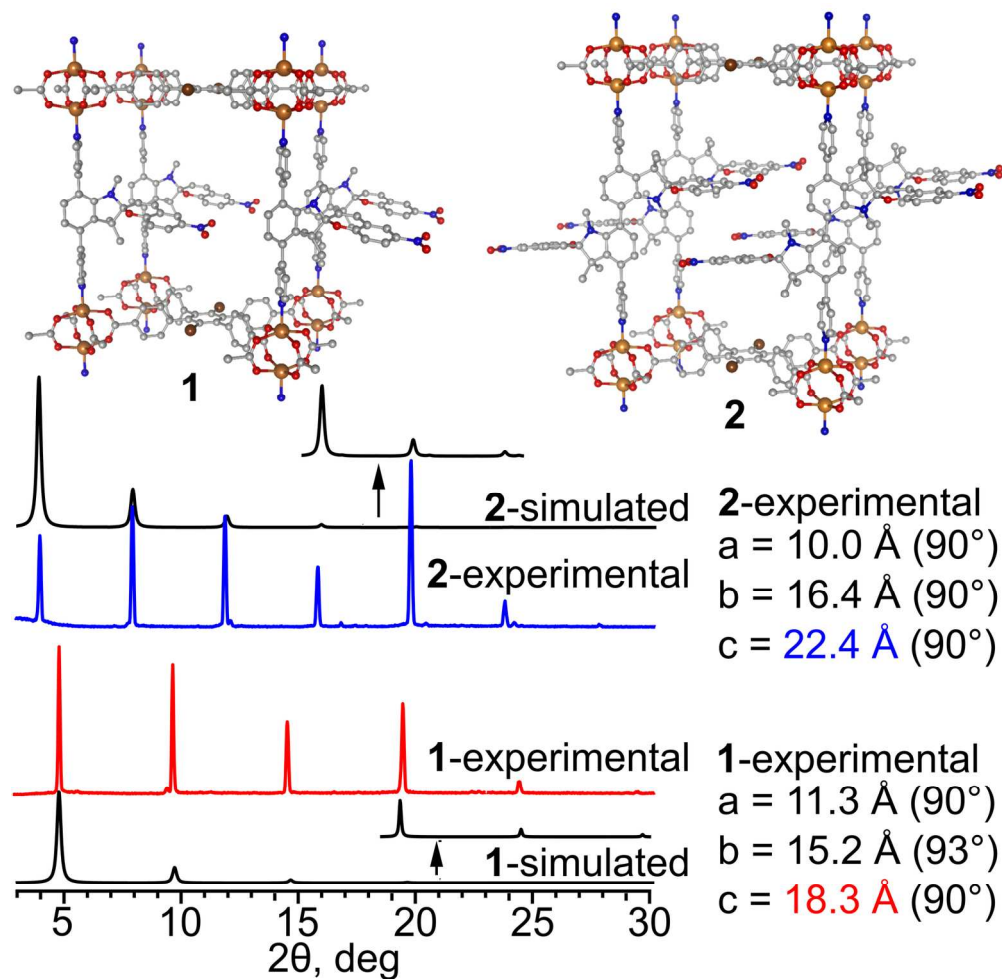


Figure 4. (top) Single-crystal structures of 1 and 2 with simulated spiroopyran moiety located in the pores. (bottom) The simulated and experimental PXRD patterns of MOFs 1 (red) and 2 (blue). The colored text shows the increase of interlayer distance for each MOF, which is in agreement with the sizes of the installed photochromic linkers.

79x77mm (600 x 600 DPI)

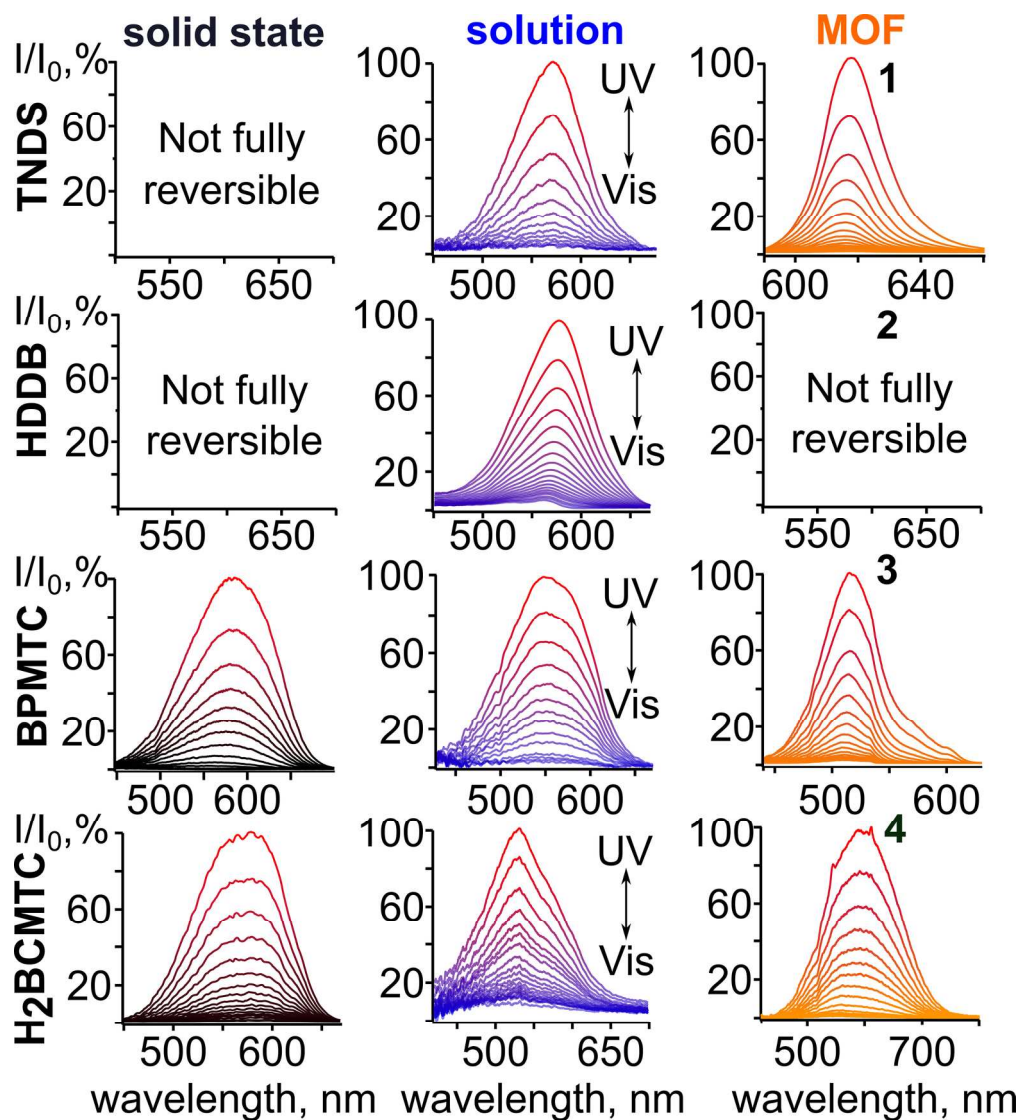


Figure 5. Normalized absorption plots of TNDS, HDDB, BPMTc, H₂BCMTc in the solid state, solution, and coordinatively immobilized inside MOF upon irradiation with UV and visible light.

92x102mm (600 x 600 DPI)

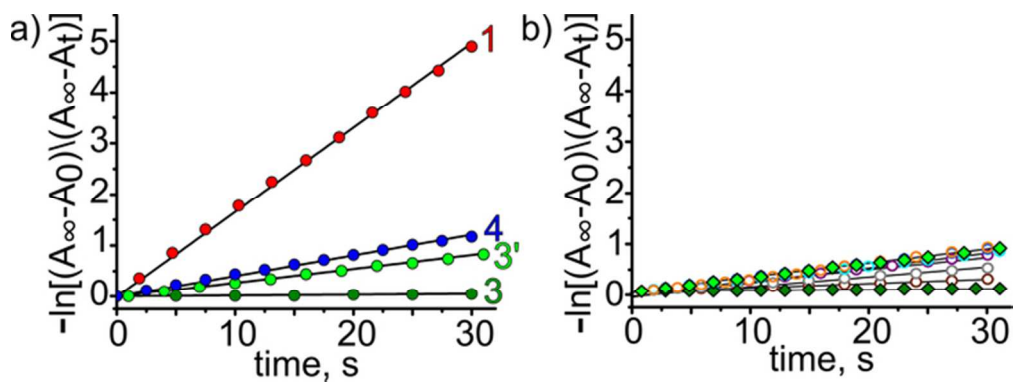


Figure 6

30x11mm (600 x 600 DPI)

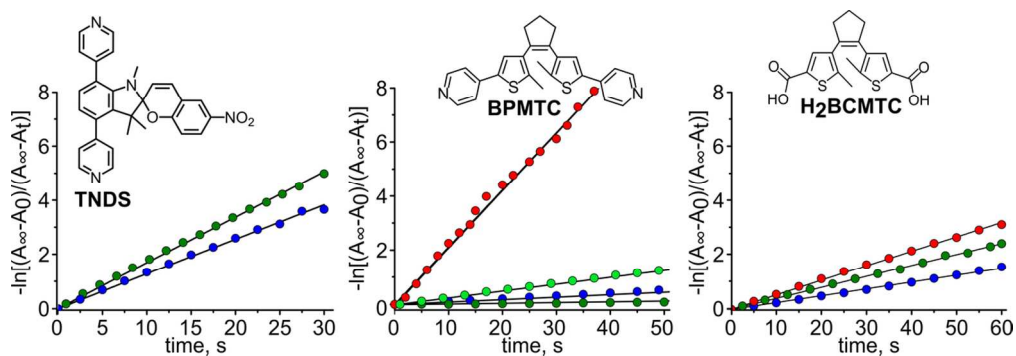


Figure 7. The cycloreversion kinetics of TNDS, BPMTC, and H2BCMTC as a solid (red), solution (blue), and immobilized in a MOF (green) upon irradiation with visible light.

58x20mm (600 x 600 DPI)

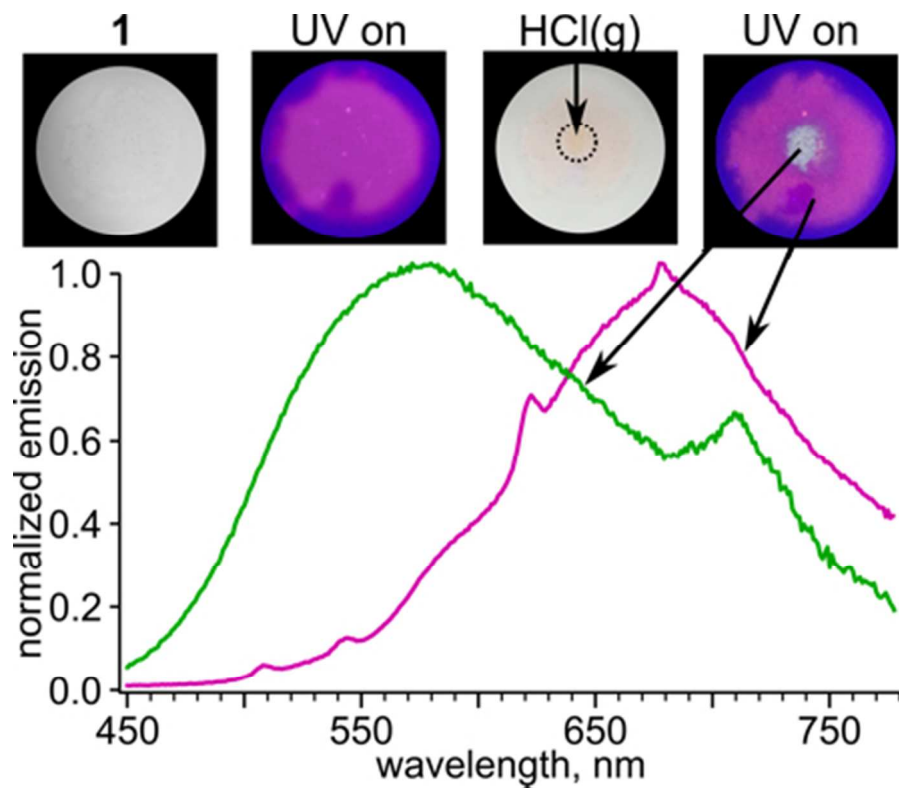
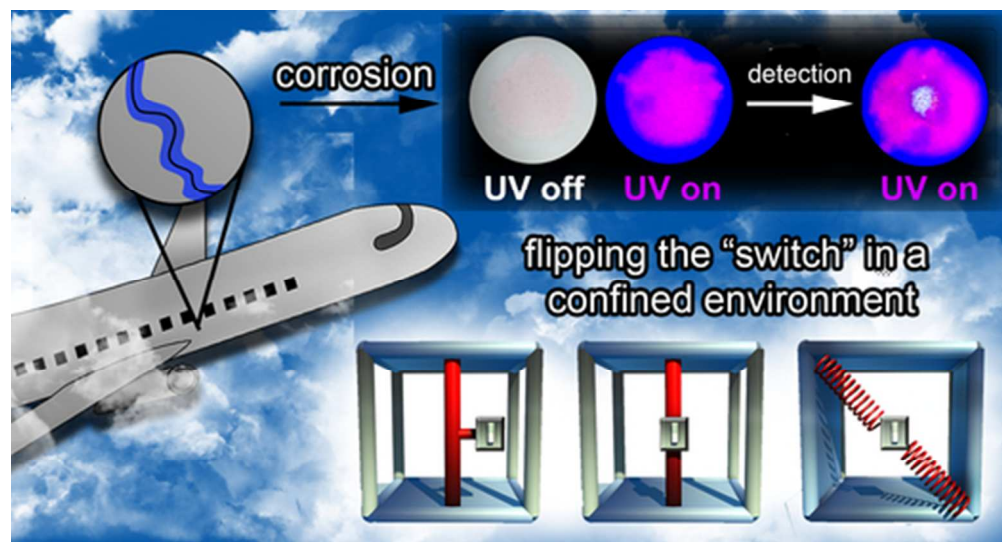


Figure 8

75x65mm (150 x 150 DPI)



TOC

44x23mm (300 x 300 DPI)